Master's thesis

NTNU
Norwegian University of Science and Technology
Faculty of Information Technology and Electrical Engineering
Department of Electric Power Engineering

Siri Faremo Haukvik

Comparison of iron loss calculation models including rotational loss

Master's thesis in MTENERG
Supervisor: Robert Nilssen
June 2020

NTNU
Kunnskap for en bedre verden

Siri Faremo Haukvik

Comparison of iron loss calculation models including rotational loss

Master's thesis in MTENERG
Supervisor: Robert Nilssen
June 2020

Norwegian University of Science and Technology
Faculty of Information Technology and Electrical Engineering
Department of Electric Power Engineering

NTNU
Norwegian University of
Science and Technology

Comparison of iron loss calculation models including rotational loss

Siri Faremo Haukvik

Abstract— **This thesis aims to investigate iron loss prediction models for electrical machines, with a desire to identify fast and simple models with acceptable accuracy for industrial use. A thorough literature review is presented to provide overview of loss calculation methods, where particular focus is given to the loss separation concept. Methods for coefficient determination is studied, both for constant and variable coefficients. Further expansions for including rotational losses through use of orthogonal components and expressions for rotational loss density is explored and selected for implementation. The Modified Steinmetz Equation (MSE) and Generalized Steinmetz Equation (GSE) are also implemented and compared. All calculations are based on publicly available material data and generic information. MATLAB is used for coefficient extraction, and all loss analyses are run solely using COMSOL.**

A variable coefficient method including rotational loss is shown to be most accurate for the two COMSOL models, being a synchronous hydro generator and a MW high speed permanent magnet machine. Accounting for rotational flux loci through calculation over orthogonal axes is seen to be crucial to achieve accuracy in the studied machines. Including rotational loss density allows further improvement, where an average 7% deviation from measured results is found for the hydro generator over a wide range of excitation level, for a method using variable coefficients. For nominal operation, 1-2% deviation for both the hydro generator and the high speed machine is obtained, without the use of correction factors.

I. Introduction

Calculation of core losses in electric machines has been a topic of research for over hundred years. Still, there is no standard method that is fit for all purposes. Optimal choice of method can be geometry-, material- and application dependent. However the method selection is often limited by available material data provided by the material manufacturer [1]. Common methods for evaluating iron losses can need corrections to measured results by a factor as high as 3 [2]. Thus, there is a need for sufficiently simple, nevertheless acceptably accurate, methods for use in machine design.

Losses in electrical machines originate from mechanical aspects (friction and windage), resistance in conductors (copper losses) and electromagnetic losses. Electromagnetic losses can refer to losses in the stator and rotor iron, or losses induced in other conductive materials, like in the magnets of a permanent magnet machine. Whereas mechanical and copper losses can be calculated with high precision, electromagnetic losses are still challenging [1]. Iron losses are particularly complex to predict due to the many phenomena impacting the losses, and the interdependence between physical factors. Calculations are also difficult to validate, as iron losses cannot be measured directly [1]. Eddy current losses in stator windings due to slot leakage flux and rotor surface losses from eddy currents and slotting harmonics are examples of electromagnetic losses usually excluded in loss calculations, but not withdrawn from measurements, therefore not separated from stator iron measurements [3].

A common simplification when calculating iron losses is assuming the flux is unidirectional and purely sinusoidal. However, in rotating machinery, it is neither. Rotating machinery has a two-dimensional flux, meaning the flux density vector rotates within the lamination plane[4]. This effect appears most prominently in the inner and outer corners of the teeth, and in the transition area from teeth to yoke [2]. The rotational flux can be observed by a 2D representation of the flux loci, where loci can form the shape of an ellipse, rectangle or lemniscape, depending on the geometry influence on flux flow in the relevant point [2].

However, as the alternating flux has standardized measurement techniques and requirements for how material manufacturers should provide loss density information, no standards exist for rotational flux. Rotational flux is generally challenging to measure and it can be difficult for machine designers to obtain sufficient data for loss calculations [4].

Including rotational losses in the calculation can be important not only for determining the level of overall losses, but also to identify potential hot spots in the iron [3].

Temperature has been seen to impact permeability and resistivity, thus impacting several aspects of iron losses [5]. Methods to couple thermal analysis with iron loss calculations have been developed to incorporate this effect and provide accurate thermal analysis [6].

Some iron loss calculation methods are based on the assumption that the flux density is sinusoidal. However, low-frequency harmonics can occur due to slotting effects and winding configuration [7]. Moreover, higher harmonics induced by drive systems can also drastically increase losses. Inverter fed machines can experience supply currents that are far from sinusoidal, where local maxima and minima in the supply current can induce *minor hysteresis loops*[8][9]. The loss increase is particularly high for systems with low switching frequency, due to a high degree of waveform distortion [8], and for PWM waveforms with the combination of bipolar switching and low modulation index [10].

At higher frequency operation, losses may also be impacted by skin effect causing a redistribution of flux in the lamination[11].

Degradation of magnetic properties occur during machine manufacture processes, leading to increased losses [1]. The cutting of laminations induce mechanical stresses that affect the hysteresis curve. Shearing stresses influence several microscopic phenomena in the material [12][13], leading to a reduction of permeability near the cut edge [14][15][16]. In

addition to the direct impact of the wider hysteresis loop, the tooth center losses are also increased due to the extra polarization needed to magnetise the edges [13]. The loss increase at the cut edge is larger for higher frequencies [15][16]. Moreover, the stacking and housing assembly introduce mechanical and thermal stresses that can damage the lamination insulation [2]. As the loss data supplied by material manufacturers is measured on unprocessed material, it might not be an accurate representation of the magnetic properties found in the final assembled machine [17].

The data supplied by material manufacturers is often found using standardised test procedures such as Epstein frame, where a flat material sheet is magnetised from a purely sinusoidal and unidirectional flux [18]. From this, iron losses are measured for a specific frequency and flux density. It is clear that a test under such simple conditions does not incorporate all the above described phenomena. This leads to questions regarding the limitations of the material data applicability, and whether material data can be applied in particular ways that provide more accurate estimations than others.

This thesis will focus on iron loss models forming a foundation for loss calculations using finite-element analysis, with expansions for including low-frequency harmonics and rotational losses. It is assumed no minor loops are present, and all calculations are performed for laminated cores. Section II will define underlying theory for iron losses. Section III will present a literature review on the traditional iron loss calculation methods, where two main concepts and variations of these are selected for further study. Section IV will describe commonly used methods for including rotational losses, and two methods are selected for implementation. Section VI and VII will present the method and results for implementation of the selected models in a prototype hydro generator model made in COMSOL Multiphysics 5.5. The methods were also implemented in a model of a high speed permanent magnet motor developed in the project preceding this thesis [19], where explicit methods for this model and the results are presented in section VIII. The project [19] also included an identification of relevant background material for the iron loss literature review. Sections II and III are based on this work and supplied with more extensive research.

II. Properties of ferromagnetic materials

Two main concepts form the basis of iron loss theory: The hysteresis loop and eddy currents. Although viewed as separate phenomena, they are closely related, which will be explained through the existence of *magnetic domains*.

A. Hysteresis loss

The history-dependent relation between field intensity H and flux density B is known as *hysteresis*. This history-dependence can be observed in the *hysteresis loop*, generated by applying an external field with alternating polarity to a ferromagnetic material. It is seen that when the external field changes polarity, the relation between B and H will not follow the same magnetisation curve as during initial magnetisation, resulting in a gap in the magnetisation curve. This area represents the energy used to change flux polarity in the material, and is called the *hysteresis loss*. When ac current is applied, this hysteresis loss occurs for each electrical period, due to the continuous change of direction in magnetic field [20]. A typical representation of a hysteresis loop is illustrated in figure 1.

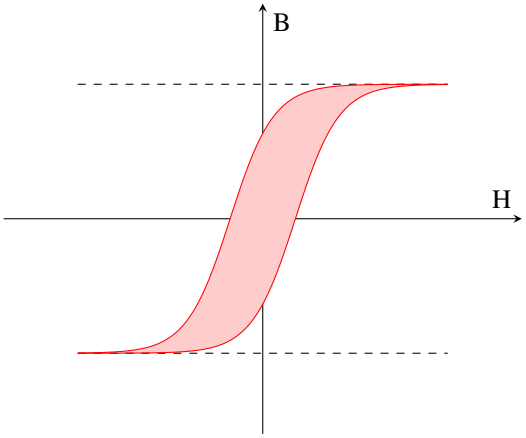

Fig. 1. Typical representation of a hysteresis loop, where the red area indicates the loss per ac cycle

B. Eddy currents

From Faraday's law it is known that a material exposed to an external magnetic field will produce a current generating an opposing magnetic field. This is the origin of the well known *eddy currents*, inducing losses in the material due to resistivity in the iron. The losses are dissipated as heat. The eddy current losses are greatly limited in electric machine cores by the use of laminations, as eddy current losses are proportional to the size of the current flow loop [20]. It can be assumed all losses in ferromagnetic materials originate from eddy currents, however it is the distribution /localisation of the current loop that determines how the losses are observed. [21]

C. The nature of magnetic domains

A ferromagnetic material consists of many small regions called *magnetic domains*. Within a magnetic domain, the magnetic field from each atom points in the same direction. When a ferromagnetic material is not magnetized, the fields from the domains point in random directions, making the piece of material appear to have no flux. Applying an external field to the material, the domains pointing in the direction of the external field will grow by shifting the *domain walls*, which are the boundaries separating the domains. This creates a positive feedback leading to increased magnetic field strength. With the increasing external field strength, whole domains reorganize and align with the field, until all atoms are aligned and the material is *saturated* [20].

The moving of domain walls is referred to as the *Barkhausen effect*, and an occurrence of this is called a Barkhausen jump. The energy released during a Barkhausen

jump is irreversibly transformed to heat by the occurrence of very localized eddy currents. The structure of the magnetic domains is determined by a combination of external and internal forces, where the external is the applied field, and the internal is a balance between several competing energy terms. These internal energy terms will not be further described in this thesis, but are described in detail in [21]. At a temperature above zero and the existence of an external field (however low the rate of change), the energy balance within the domains become unstable, making the walls shift. During very low rate of change of the external field, a Barkhausen jump occurs during such a short time relative to the change in the external field, that it can be viewed as independent of the frequency. This is in some theories referred to as *rate-independent hysteresis (quasi-static hysteresis)*. However, it must be stressed that this is an approximation. The Barkhausen jumps are also related to rate of energy dissipation and thermal fluctuations, therefore never completely independent of time. During *rate-independent hysteresis* the occurrence of the Barkhausen jumps is stochastic, due to the complexity of domain structures and the structural disorder of the internal forces [21].

However, as the rate of change of the external field increases, the stochastic behaviour ceases and a clear dependence of the rate of change can be observed. This is due to the duration of the Barkhausen jump relative to the variation of the external field no longer being so small that it can be viewed as independent. A widening of the hysteresis loop can be observed when the frequency is increased, which is related to the increased amount of eddy currents circulating in the material. The distribution of eddy currents is seen to be dependent both on the shape of the material (lamination), and on the moving domain walls, where currents seem to circulate around the moving domain walls [21].

III. Iron loss calculation methods

An extensive literature review has been conducted to provide an overview of relevant loss calculation methods and to characterise their advantages and disadvantages.

A. Classical iron loss calculation methods

There are several methodologies for calculating iron losses. Roughly, they can be divided into three main groups. The first group is methods based on the original Steinmetz equation, which was a very early loss calculation model. The second are loss separation methodologies, aiming to separate the iron losses by dependencies of flux density and frequency into static and dynamic parts. Lastly, there is hysteresis models describing the hysteresis behaviour mathematically or empirically, finding the loss as the area of the dynamic hysteresis loop [1].

1) The Steinmetz equation: The original Steinmetz equation (1) was proposed in 1884, and alterations and improvements have been suggested many times since then. The method is based on empirical observations and assumes a specific iron loss density p [W/kg], and three coefficients C_{se}, α, β that are dependent on material data, and fitted to measurements. The original equation is only valid for sinusoidal excitation.

$$p = C_{se} \cdot f^{\alpha} \cdot \hat{B}^{\beta} \tag{1}$$

Generally, the Steinmetz based methods are quick and require little knowledge about the material. However, the Steinmetz coefficients have been shown to vary with frequency [1].

Improved versions of the Steinmetz equations accounting for arbitrary waveform, DC-bias and major and minor hysteresis loops have been developed. A thorough review of these methods can be found in [1].

The modified Steinmetz equation (MSE) has been given much attention, and is based on the concept of introducing an equivalent frequency accounting for harmonics. It was introduced in [22], and originally intended for use in power electronic components. The MSE is given in equation 2, where 2b is the calculation of the equivalent frequency. ΔB is the peak-peak value of B, and C_{se}, α, β are the coefficients fitted from the original Steinmetz equation (1).

$$p = C_{se} \cdot {f_{eq}}^{\alpha-1} \cdot \hat{B}^{\beta} \cdot f \tag{2a}$$

$$f_{eq} = \frac{2}{\Delta B^2 \pi^2} \int_0^T \left(\frac{dB}{dT} \right)^2 dt \tag{2b}$$

Some advocates for the Modified Steinmetz Equation argue there is no physical basis for separating dynamic and static losses, and iron losses should therefore be calculated in collected form [23].

The Generalized Steinmetz equation (eq.3) is a bit newer than the MSE, and is based on instantaneous power loss. It includes DC-bias sensitivity, which is an advantage compared to the MSE. A disadvantage is that it can have reduced accuracy if the third or another close harmonic becomes significant[1]. The Steinmetz coeffient C_{SE} must be altered by equation 3b for GSE, which works so that equation 3a solves back into the original Steinmetz equation (1) for sinusoidal flux.

$$p = \frac{1}{T} \int_0^T C_{GSE} \left| \frac{dB}{dT} \right|^{\alpha} \cdot |B(t)|^{\beta-\alpha} dt \tag{3a}$$

$$C_{GSE} = \frac{C_{SE}}{2\pi^{\alpha-1} \int_0^{2\pi} |cos(x)|^{\alpha} \cdot |sin(x)|^{\beta-\alpha} dx} \tag{3b}$$

Another advancement is the improved Generalised Steinmetz equation (iGSE) which includes minor hysteresis loops [24].

2) Loss separation: Loss separation is very commonly used for calculations in rotating machinery, being founded on relatively simple post processing.

The first loss separation theory was proposed by Jordan in 1924, and was based on the concept of separating the losses to a static and a dynamic part, as presented in equation 4. The static losses were the hysteresis energy

loss when the frequency approaches zero, and the dynamic losses were generated by the eddy currents circulating in the lamination[1].

$$p = K_h \cdot \hat{B}^2 \cdot f + K_e \cdot \hat{B}^2 \cdot f^2 \tag{4}$$

The eddy currents were assumed to distribute homogeneously, and could therefore be calculated analytically by dependencies of material specifications, as in equation 5.

$$K_e = \frac{\sigma \pi^2 t^2}{6\delta} \tag{5}$$

where σ is the material electrical conductivity, t is the lamination thickness and δ is the material density in $\frac{kg}{m^3}$. Eddy current losses calculated using the coefficient in equation 5 are often referred to as *classical eddy current losses*.

Using Jordan's equation today, both coefficients K_h and K_e are often fitted to material data based on a least-square-method [5].

An expansion of this method was proposed by Bertotti in 1988, introducing a third term to the loss separation theory: The *anomalous(excess)* loss component [25] [26]. This component was introduced to account for inhomgenous distribution of eddy currents. Bertotti argued that iron losses are so complex due to the dependence of geometry and material properties in both space and time, that it can only be treated statistically. Therefore, breaking down the losses into three components would allow calculating the separate contributions over different scale. The microscopic phenomena inducing losses independent of time (Barkhausen jumps) would be represented by the quasi-static hysteresis losses, the geometry-dependence would be represented through the homogeneous distribution of eddy currents in the lamination, and the eddy currents induced around moving domain walls were represented by the anomalous component through expressing the statistical behaviour of the domain wall movement [21]. It should be remarked that the three components are treated as statistically independent based on empirical data and to ease calculation, which does not mean the losses are physically independent of each other. A full derivation of Bertotti's loss separation theory can be found in [21].

The Bertotti model is presented in equation 6, where P is the total iron losses, P_h is the quasi-static hysteresis losses, P_e is the classical eddy current losses and P_a is the anomalous losses.

$$p = p_h + p_e + p_a$$

$$p = K_h \cdot \hat{B}^{\alpha} \cdot f + K_e \cdot \hat{B}^2 \cdot f^2 + K_a \cdot \hat{B}^{1.5} \cdot f^{1.5} \tag{6}$$

K_e, K_h, K_a and α are constants depending on material. α is usually between 1.6 and 2.2 for ferromagnetic materials and alloys [1].

A generalised version of Bertotti's equation was proposed by Fiorillo and Novikov [27], allowing calculation for arbitrary flux waveform by time-domain or frequency-domain models. The coupling of equation (6) and a Fourier transform to sum up the contributions from each harmonic in the magnetic field is a popular approach [28].

Advantages of Bertotti's method is simplicity, stability, and giving quite good results within some ranges of frequency and voltage [29]. It has been shown that the Bertotti-method is quite accurate for lower flux densities, but deviates from measurements at higher flux densities [29]. In [29], this is explained by the neglect of skin effect, minor loops and rotational losses.

The Bertotti method has many similarities to the Steinmetz methods, and might be viewed as a Steinmetz derivation. Loss separation is, like Steinmetz, based on evaluating loss using frequency, induction level, and curve fitted constants to represent material properties. Like the Steinmetz equation, Bertotti's method has been extended and modified in innumerable ways and works, and the modifications show many overlapping concepts to Steinmetz derivations. Therefore, to clarify, any method based on separating loss components will in this thesis be referred to as a loss separation method, although it might include ideas originating from a Steinmetz derivation.

3) Hysteresis models: The last main group of models are the hysteresis models. These aim to describe the hysteresis loop, and generally give more accurate results [1]. However, they also require more information about the material and the flux density wave forms. Thus, Finite Element Method(FEM) implementation is more complicated [1].

Thoroughly studied hysteresis models are the Preisach model and the Jiles Atherton model[30], which have been modified several times after their original publication. Derivations of the Preisach model into generalized and vectorial form is extensively described in [31]. Jiles Atherton's model extended for anisotropic material was proposed in [32] and a vector generalisation of the Jiles-Atherton model allowing three dimensions was proposed in [33]. A review of hysteresis models can be found in [1].

In [34] a hysteresis method calculating instantaneous loss is presented, thereby being able to evaluate arbitrary waveforms. The method requires input data from a measured hysteresis loop, and is concluded to be simple and give accurate results. In [35], a dynamic hysteresis model is introduced, including minor loop compensation. The model is based on an inverse Preisach model, but transformed to a dynamic form.

B. Enhancement of Field Solutions in FEM

The need for accurate field solutions incorporating 3D effects and including losses can be discussed. Fratila et.al [36] compared using a 2D and a 3D model to compare the effect of neglecting end-ring and damper bar losses, where no significant difference was found between the 2D and 3D simulation. Representing 3D-effects in the laminations can be done using *homogenisation*, where a laminated core can be replaced by a bulk material with the same geometry and similar electromagnetic behaviour [37]. In [38], a homogenization method for modelling laminated iron cores by 3D

finite-element time-stepping is proposed, and validated for a 3D-axisymmetric case. The model makes it possible to include the skin effect and fill factors.

In [29], a method incorporating the losses into the magnetic field solutions is developed through a hybrid model of the statistical loss separation and the mathematical hysteresis loops. This was concluded to be relatively accurate, stable and efficient for loss estimations in a 37 kW induction machine. A continuation of this work is presented in [39], where the effect of neglecting iron losses in the field solution is investigated. It is found that such neglect could induce up to 15% discrepancies from the measured results.

C. Scope selection

As the aim of this thesis was to investigate methods providing quick analysis for industrial use, hysteresis models and advanced field solutions were considered to be too complex. Based on the literature review where loss separation models seem to be the most popular selection for rotating machinery, loss separation is selected as a main concept fit for further investigation of alterations and adaptions.

D. Determination of coefficients for loss separation

Loss separation methods require certain coefficients to be set using experimental data. The quality and amount of this data can be determinative for the accuracy of the loss calculation [28] [1].

1) Selection of frequency range: For coefficients determined by curve fitting, the frequency range on the input data can have impact on the coefficient accuracy. It has been seen that the loss estimation deviates more from the measured results outside of the range of frequency and flux density used for finding the coefficients [36]. This can apply particularly for high speed machines, as material data is often given in the range from 50 Hz - 400 Hz or similar. [40] found that using a frequency range close to the intended operating area might be more accurate than having a very wide range, even though the data points are fewer. This is explained by high frequency data tending to dominate the solution and make the constants less accurate for operation at lower frequencies

In [36], it is recommended using at least three sets of frequencies: low frequency for quasi-static evaluations, and data for the fundamental frequency and a prominent harmonic to fit K_e and K_a.

2) Hysteresis loss by quasi-static conditions: To evaluate the hysteresis losses by quasi-static conditions according to Bertotti's theory, the frequency must be so low that all dynamic losses can be assumed negligible. When this data is obtained, coefficients K_h and α can be fitted from equation 7, where w is the energy loss density [J/kg].

$$\lim_{f \to 0} w = K_h \cdot \hat{B}^{\alpha} \tag{7}$$

Use of this approach is seen in amongst others [36] and [41], where measurements at respectively 5 Hz and 2 Hz are used.

However, many works using Bertotti's equation (6) does not specifically mention whether coefficients are fitted at quasi-static conditions (eg. [42]), and others use pure curve fitting [28]. There are also several works where α is set to 2, and not found from loss data [43].

3) The anomalous loss component: In the original research published by Bertotti [25], the anomalous loss component is estimated by a number of statistical variables. The statistical analysis is based on the knowledge that when a Barkhausen jump has occurred in a given region, there is increased probability that a new Barkhausen jump will occur in a neighbouring region. This can be described by the term *correlation regions*, where *n* is the number of active correlation regions [21]. Regions of high interaction between magnetic domain walls are often in literature referred to as *magnetic objects*. Statistical theory regarding the magnetic objects can be derived, and the parameters n and V define how several microstructural features influence the losses [21]. n_0 is the number of simultaneously active magnetic objects when the frequency goes to zero. V_0 represents the statistical behaviour of the magnetic objects and has the unit of a magnetic field.

In its simplest form, the anomalous loss component can be expressed as in equation 8. This method is seen used in [42].

$$p_a = 8.76\sqrt{\sigma S G V_0} \cdot \hat{B}^{1.5} \cdot f^{1.5} \tag{8}$$

where σ is the conductivity, S is the lamination cross section and G is a dimensionless constant of 0.1356. Equation 8 is valid for sinusoidal excitation and only for particular materials, where many materials frequently used for electrotechnical applications apply, for example Si-Fe [21]. Equation 8 is also derived by finding the averaged losses over the hysteresis loop. When the anomalous losses are expressed as in equation 8 and hysteresis coefficients are fitted at quasi-static conditions, V_0 is the only unknown needing to be curve fitted to material data.

In [41], more generalized models for the anomalous loss component is investigated. The hysteresis loss components is evaluated at quasi-static conditions, the eddy current coefficient is found classically (equation 5), and the anomalous losses are calculated using 9 and 10, and then results are compared. Both equations 9 and 10 assume sinusoidal flux. Unidirectional flux is assumed for all derivations in this work.

$$p_{a_{Kowal1}} = 2\hat{B}f\left(\sqrt{{n_0}^2{V_0}^2 + 2\pi^2\sigma G S V_0 \hat{B}f} - n_0 V_0\right) \tag{9}$$

where n_0 and V_0 are functions of $\hat{B}$ fitted to loss measurements.

$$p_{a_{Kowal2}} = c\hat{B}f\left(\sqrt{1 + e\hat{B}f} - 1\right) \tag{10}$$

where c and e are constants curve fitted through least-square method. The results show large deviations in accuracy

for the constant coefficient method, as presented in figure 2, where simulation is performed on a fully processed non-oriented steel with lamination thickness 0.3 mm at 50 Hz. Similar tendencies were seen at 400 Hz, however lower error at low and high induction level and higher errors at medium induction level.

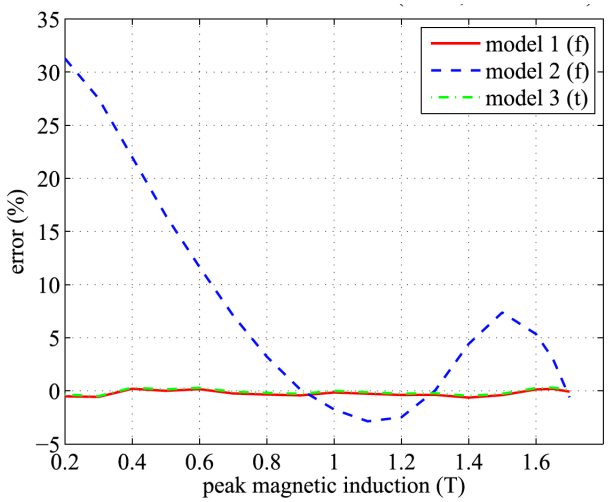

Fig. 2. Comparison of error induced when using the two equations above for measurements at 50 Hz and sinusoidal flux waveform [41]. Model 3 is a time domain model, which will be discussed later in this thesis

However, in many works, none of these statistical values are mentioned. Commonly, the anomalous loss term is simply found using the simple relation in equation 6, where K_a is a constant.This is seen in [28], [42], [36]. In other analyses, this term is set to zero based on material properties [43].

4) Variable coefficients: Much research on introducing variable coefficients in the Bertotti equation has been performed, in early phase lead by Ionel et.al [44]. The investigation of several steel samples, as well as FEA on two example machines was seen to give very accurate loss evaluations when using variable coefficients as in equation 11 [44]. This model is called the *VARCO*-model. The anomalous loss term was set to zero, justified by the separation of classical eddy currents and anomalous losses being "questionable". It was stressed by the authors that this does not mean the anomalous loss term does not exist, just that it might not be proportional to the power coefficient of 1.5. To separarate this eddy current loss term from the classical eddy current loss term, it will be referred to as K_d, for *dynamic*. K_d, K_h and α were set to third-order polynomials fitted to measured curves in a frequency range from 20Hz -2kHz, varying with frequency and flux density.

The effect of setting α to 2, while still representing K_d and K_h as polynomials was also studied. When α was set to a constant, K_h was expanded to also vary with flux density. This method showed acceptable accuracy and much better computational efficiency. Additionally, it was also validated through measurements, thus being the choice of recommendation by Ionel et al. This method is referred to as the *CAL2*-method (equation 12). Interestingly, it was found in [44] that the average value of K_d has a maximum of 14% deviation from the value found using (5) for the three measured materials (for CAL2).

$$p_{VARCO} = K_h(f) \cdot \hat{B}^{\alpha(f,B)} \cdot f + K_d(f,B) \cdot \hat{B}^2 \cdot f^2 \quad (11)$$

$$p_{CAL2} = K_h(f,B) \cdot \hat{B}^2 \cdot f + K_d(f,B) \cdot \hat{B}^2 \cdot f^2 \quad (12)$$

In the CAL2 model, a linear relation for the specific core loss ratio is used to demonstrate the coefficient dependency on flux density. By transforming equation 12 to the equation given in 13, an approximate linear relation can be seen. This relation is shown for three levels of flux density in figure 3, and shows a clear variation with flux density.

$$\frac{p}{f \cdot \hat{B}^2} = K_h(f,B) + K_d(f,B) \cdot f \quad (13)$$

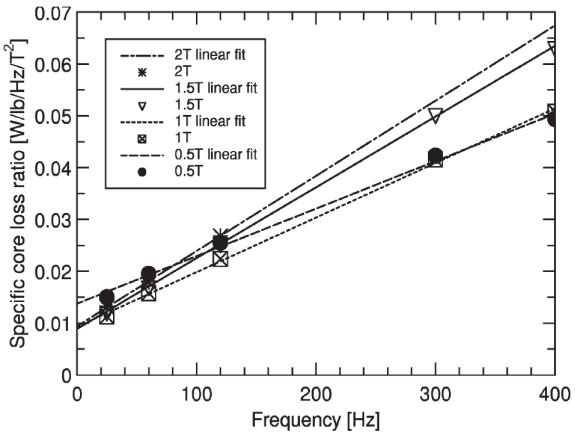

Fig. 3. Linear fit of specific core loss ratio per flux density presented in [44]. The figure shows a clear dependency of flux density for the coefficients

The authors admit to the fact that the *VARCO* and *CAL2* models are "best-fit" models, and thus their physical interpretation is limited. The exact separation of losses can not be guaranteed by this model, however the authors claim this is a problem for constant coefficients as well. It is also pointed out that the contributions from the anomalous loss component might not only be represented by the eddy current component, but possibly also somewhat in the hysteresis component. It should also be noted that no quasi-static analysis is performed in this method.

The CAL2-model was further explored by Dlala et.al [45], where the physical basis for variable coefficients is investigated. In this work, it is stressed that finding correct coefficients is key for accurate core loss analysis, however the method for identifying coefficients must be chosen with care. It is claimed that the power loss is not appropriate to use for identifying coefficients, but the energy loss should be used:

$$w = \frac{p}{f} = K_h \cdot \hat{B}^2 + K_d \cdot f \cdot \hat{B}^2 \quad (14)$$

From the energy equation (14) it is seen that the hysteresis energy loss is independent of frequency, and the hysteresis coefficient should thereby not be allowed to vary with frequency. The dynamic loss coefficient K_d, on the other hand, *can* be allowed to vary with both flux density and frequency, as the classical energy loss is dependent on both of these. It is therefore concluded that K_h should only vary with peak flux density, and K_d should vary with peak flux density and frequency. This supports the quasi-static theory used in Bertotti. The method further argues that as the frequency approaches zero, the static energy loss can be read out of equation 14. The quasi-static condition is modelled using a linear fit similar to the one presented by Ionel et.al. in figure 3. Thus $K_h(\hat{B})$ is determined for each level of flux density, and then $K_d(\hat{B}, f)$ can be determined for every $\hat{B}$ and f by reverting equation 14 and inserting $K_h(\hat{B})$, thus finding a table of values for K_h and K_d. Coefficients are then interpolated using cubic spline algorithm. The analysis is then performed using Fourier analysis, and loss is found per harmonic. Similar method (eq. 12, $K_h(\hat{B})$, $K_d(\hat{B}, f)$) with Fourier analysis and coefficients varying with harmonics is seen used in research on a MW high speed permanent magnet machine by Zhang et.al.[43]. However, no method for identifying coefficients is described in this work.

5) Comparison of methods for coefficient determination: In [5], several variations of the loss separation methods were compared to measurements on a lamination ring specimen under alternating sinusoidal flux:

1) The Bertotti equation (6) combined with coefficients determined from the classical eddy current coefficient K_e (equation 5) and curve fitting α, K_h and K_a over a range of flux densities and frequencies.
2) The Bertotti equation (6) with coefficients K_h and α fitted to measurements from a DC hysteresis test and calculating K_e by (5), thereafter fitting K_a to material data
3) The Jordan model (4) where K_e is replaced by K_d, a coefficient curve fitted to measured values to represent the total sum of dynamic losses (classical eddy current and anomalous)
4) The CAL2-model (12) with variable coefficients as introduced in [44]. The variation with frequency is considered by defining a low- and high-frequency set of polynomials, where the low frequency range used data for 50, 200 and 400 Hz, and the high frequency used data for 600, 800 and 1000 Hz.

It was found that the CAL2-model was much more accurate than the others. Whereas the accuracy of all the three other models varies significantly with frequency and flux density, whereas the CAL2 model showed good accuracy over a wide range of frequency and flux density (50-1000 Hz, 0.6-1.173 T). The average prediction relative errors were respectively, 11.3 % , 10.3 %, 10.7% and 2.4%. It is seen that the improvement in accuracy of fitting hysteresis coefficients using static conditions is very small compared to the simple curve fit method. Moreover, the accuracy is the nearly same for as for the Jordan model with only two coefficients, both fitted.

However it should be remarked that measurements are performed on a very simple geometry (ring specimen), not an electrical machine.

E. Calculation in the time domain for loss separation

To include harmonics in the loss calculation, an alternative to the Fourier transform is calculation in the time domain. As FEA is built on time-stepping, equations that calculate over continuous or discrete time can be more efficient, reducing the need for post-processing by removing the Fourier transform step [28].

1) Constant coefficients: In [28], a simple version of the Bertotti equation in the time domain is used (equation 15). The eddy current and anomalous losses are calculated from a time derivative of the flux, as they are induced due to the changing flux density in the material. The hysteresis losses are dependent on peak flux density magnitude. The extension of the original Bertotti equation (6) into the version for generalized flux waveform as seen in equation 15 was first proposed by Fiorillo and Novikov [27] in 1990.

$$P = p_h + p_e + p_a$$

$$p_h = K_h \cdot \frac{1}{T} \cdot \hat{B}^{\alpha} \tag{15a}$$

$$p_e = K_e \cdot \frac{1}{2\pi^2} \frac{1}{T} \int_0^T \left| \frac{dB}{dT} \right|^2 dt \tag{15b}$$

$$p_a = K_a \cdot \frac{1}{8.76} \frac{1}{T} \int_0^T \left| \frac{dB}{dT} \right|^{1.5} dt \tag{15c}$$

The same methodology (equation 15) is seen in [36], where the method is validated through measurements.

2) Comparison between time- and frequency-domain model: In [46], iron loss calculation using FEM for a 2.1 MW permanent magnet synchronous generator is made with two different methodologies, comparing a frequency- and a time-domain methodology. Both models find hysteresis loss by quasi-static conditions and classical eddy current losses (equation 15b for time domain). A large difference is in the anomalous loss term, where the frequency domain model uses equation 10, whereas the time-domain model uses equation 16. A difference between these is that the time domain model uses n_0, V_0 dependent on $\hat{B}$, whereas they are constant in the frequency domain model. Both models are further expanded to include rotational losses, and the time domain model also to include PWM harmonics. It is concluded that the frequency-domain model underestimates the losses.

$$p_a = \frac{1}{2T} \int_0^T \left(\sqrt{{n_0}^2 {V_0}^2 + 4\sigma G S V_0 \left| \frac{dB}{dT} \right|} - n_0 V_0 \right) \left| \frac{dB}{dT} \right| dt \tag{16}$$

As the frequency domain model uses constant coefficients whereas the time-domain model uses n_0, V_0 dependent on $\hat{B}$, it is difficult to evaluate whether the increase in accuracy is owning to the use of time domain approach or the use of varying coefficients. However, it is seen in more extensive research by the same authors that the coefficients is the main reason for loss of accuracy [41]. Comparing the frequency domain model presented in equation 9 to the time domain model in equation 16, the accuracy is very similar. These two models are equivalent in parameter input and measured both using sinusoidal flux and non-sinusoidal, for the latter case evaluating (9) using Fourier analysis to ensure comparability. It thereby seems that frequency-domain and time-domain models are equally suitable based on these works, however the time-domain-model might be advantageous based on the readiness to include PWM current and minor loop losses using the methodology presented in [46].

3) Variable coefficients in combination with time domain calculation: Ionel et.al also performed a time domain-extension of their variable-coefficient models in [44], to include non-sinusoidal waveforms. In the time domain, the coefficients are dependent only on the flux density at fundamental frequency to simplify. The eddy current loss term is shown in equation 17. As described earlier, the work in [44] studied the effect of setting α to two (*CAL2*-model), compared to expressing it as a polynomial (*VARCO*-model). Therefore, the hysteresis loss equation is somewhat different in these two models, as shown in equations 18 and 19. It should be noted that these hysteresis formulas are only valid for variable coefficients, and information about the hysteresis loops shape is required.

$$p_d = \frac{1}{2\pi^2}\frac{1}{T}\int_0^T k_d(f_1, B)\cdot\left[\frac{dB(t)}{dT}\right]^2 dt \tag{17}$$

$$p_{h_{VARCO}} = \frac{k_h(f_1)}{\pi}\frac{1}{T}\int_0^T B(t)^{\alpha(f_1,B)-1}\cdot\left[\frac{dB}{dT}\right]dt \tag{18}$$

$$p_{h_{CAL2}} = \frac{1}{\pi}\frac{1}{T}\int_0^T k_h(f_1, B)\cdot B(t)\cdot\left[\frac{dB}{dT}\right]dt \tag{19}$$

The results in [44] yields the *VARCO*-model in the frequency domain to be most accurate. The accuracy of the time-domain models seem to be lower for analyses where a higher degree of harmonics is present. This is explained by the simplification of letting the coefficients vary only with B at fundamental frequency, while the frequency-domain model finds new coefficients for each harmonic. This tendency is the same for both *VARCO* and *CAL2*.

The *CAL2*-model is further investigated in [47]. Seven variations are compared: The traditional Bertotti (eq. 6, $\alpha = 2$), CAL2 in frequency domain, including only fundamental (eq.12), CAL2 in time domain (eq. 19 and 17), CAL2 in the frequency domain including up to 11th harmonic (eq. 12 with Fourier analysis) and three extensions including PWM losses. Due to operating only under 400 Hz, it is concluded coefficients K_h, K_c need only vary with $\hat{B}$. The time domain version of CAL2 performs best, and the basic Bertotti method performs poorest, for measurements made on an inverter-driven brushless DC-motor.

4) Using coefficients extracted by frequency-domain formula in time-domain simulations: As the input data given by manufacturers is given per frequency, coefficients are usually curve fitted to frequency domain formulae. The validity of using these coefficients in time domain approaches can be questioned.

In the research by Ionel [44],the use of coefficients curve-fitted from measurements on sinusoidal flux density into non-sinusoidal fields is questioned, but not further discussed.

In [41], using coefficients derived from sinusoidal measurements in the time-domain approach is concluded to be a valid approach. However, care should be taken to which equation the coefficients are fitted to, where using discrete values of $\hat{B}$ is accurate, whereas assuming a piecewise linear $B(t)$ can induce errors as much as 16% higher than when using discrete values.

Dlala [45] claimed that as standard core loss material data is found at sinusoidal frequency, frequency domain models are best fit to represent the experimental behaviour (compared to time-domain models). No calculations or measurements were performed to support the statement.

To the authors knowledge, little other research has been published on this.

5) Comparison of methods: Due to the large variation of methodologies regarding coefficient fitting, number of components, use of statistical expressions or special effects occurring in the machine studied, it is difficult to find common ground for comparing the methods and conclude on a overall superior method.

However, as mentioned in section III-D.5, [5] found the CAL2-model to be advantageous compared to constant coefficient-models for measurements under sinusoidal flux. Using a completely different approach, focusing on excess losses, [41] also concluded coefficients should include variability for flux density, however in a much more mathematically heavy statistical form. Thereby, it seems that using variable coefficients might be advantageous. The improvement by implementing this should be weighted against the complication it induces in the calculation.

A summary of the literature review is presented in table I. It is seen that both variable and constant coefficients are commonly used. It seems to be most common to include the anomalous loss component when constant coefficients are used, where [41] is the only one using three terms and variable coefficients. Moreover, no pattern is found between the inclusion of rotational loss and the choice of including anomalous loss component or using variable coefficients. However it should be mentioned that the extensive amount of research on iron losses might not be fully reflected in this table.

TABLE I
SUMMARY OF LITERATURE REVIEW

Article	No.of comp-onents	Time/ frequency plane	Constant/ Variable coefficients	Rotational loss included
Hargreaves [28]	3	Time	Constant	Yes
Zhang [43]	2	Frequency	Variable	Yes
Ionel [44]	2	Both	Variable	No
Dlala [45]	2	Frequency	Variable	No
Kowal [41]	3	Both	Variable	No
Kowal [46]	3	Both	Both	Yes
Zhu [5]	2	Frequency	Variable	Yes
Huang [42]	3	Frequency	Constant	Yes
Fratila [36]	3	Time	Constant	Yes

Some differences between time- and frequency-domain models have been seen. Frequency domain models allow separating the loss contribution from the harmonic [29]. This is more challenging in time-domain models. Moreover, for variable coefficient methods, harmonic variations of coefficients can be taken into account if frequency domain is used [29][44]. However, in frequency domain models, the phase shift between harmonics is neglected, which can result in lower loss calculations compared to using time-domain models [11].

F. Methods selected for further study

Based on the literature review, the impact of changing from constant coefficients to variable coefficients was selected for further study. Moreover, the effect of using time-domain models compared to a fundamental frequency domain model was investigated. Additionally, two variations of the Steinmetz equation were implemented to see the difference between loss separation and calculation in collected form.

Moreover, the selection of methods for further study was based on the following criteria:

- The availability of data. Due to the unavailability of quasi-static data (specific loss measurements at sufficiently low frequency), the methods largely based on this concept was ruled out (all models in section III-D.3).
- Possibility of implementation directly in COMSOL
- Fast calculation

1) Jordan model: This model is a two-term loss separation model with constant coefficients. The frequency domain model is presented in equation 4, and the time domain model is found by replacing the eddy current loss term by the expression in 15b. The coefficient K_e is replaced by a coefficient K_d, as curve fitting is used to obtain the eddy current coefficient.

2) Bertotti model: The Bertotti method with constant coefficients is also selected for further study. Due to unavailability of quasi-static data, the α coefficient was set to 2 to limit the amount of free variables. The eddy current coefficient K_e is found by the analytical equation 5. The frequency domain formula is given in equation 6, and the time domain version is given in equation 15.

3) CAL2 method: The CAL2 method is an extension of the Jordan method, using variable loss coefficients. The equation in the frequency plane is given in equation 12 and the equation for eddy current loss in the time domain is given in equations 17. The coefficients K_h and K_d are approximated as third-degree polynomials using the relations in equations 20. The hysteresis model used in the time-domain calculations in the original work by Ionel [44] and presented in equation 19 was not used as the required hysteresis loop information was not available. This also assures the method is comparable to the Jordan and Bertotti models as described above, thereby isolating the impact of the coefficients.

$$K_h(f,B) = k_{h0} + k_{h1}\hat{B} + k_{h2}\hat{B}^2 + k_{h3}\hat{B}^3 \tag{20a}$$

$$K_d(f,B) = k_{d0} + k_{d1}\hat{B} + k_{d2}\hat{B}^2 + k_{d3}\hat{B}^3 \tag{20b}$$

The coefficients in 20 are made variable by frequency by approximating a polynomial per frequency range. In the original work by Ionel et.al. [44], this was done by finding three sets of polynomials: for low(25-400Hz), medium(400-950), and high (1050-2100) frequency range.

4) Dlala method: The method used by Dlala et al in [45] is based on the CAL2-method, but calculations are found in a point-wise form. Using equation 13, a linear approximation is found per flux density. As K_h is concluded to be independent of frequency, the values for $K_h(B)$ can be read out of the linear approximations, by setting the frequency in equation 14 to zero. Thereby, the values for K_h can be found using equation 21, and tabulated per flux density. Thus, the values for $K_c(f,B)$ can be found from reverting equation 13 and calculating per $\hat{B}$ and f as in equation 22. The tabulated values are then interpolated using cubic spline interpolation (in the work by Dlala).

$$K_h(\hat{B})\Big|_{f=0} = \frac{w}{\hat{B}^2} \tag{21}$$

$$K_c(\hat{B},f) = \frac{w - K_h(\hat{B})\cdot\hat{B}^2}{f\cdot\hat{B}^2} \tag{22}$$

The work by Dlala has not been investigated in the time domain, and the time domain version of the eddy current losses given for the CAL2 model (equation 17) is therefore used, replacing the CAL2-coefficient by the Dlala-coefficient. Therefore, only the fundamental frequency coefficient can be used, which is a disadvantage as one of the advantages by the Dlala model is neglected.

5) Dlala_sep method: Furthermore, to obtain a dataset better fit for further expansion, the Dlala-method was attempted extended to three components, as in Bertotti's loss separation. This was done by defining a curve fit per flux density using equation 23, and reading out the K_h-values using equation 21.

$$\frac{p}{f \cdot \hat{B}^2} = K_h + K_e \cdot f + K_a \cdot \sqrt{\left(\frac{f}{\hat{B}}\right)} \tag{23}$$

$K_a(\hat{B}, f)$ was thus found by altering equation 22 to include the classical eddy current losses, as given in equation 24. The coefficient for classical eddy current losses K_e was found from the analytical expression in equation 5. Thereby, the eddy current coefficient was no longer variable, but the anomalous coefficient was. Assuming skin effect is negligible, is is likely the eddy current does not need to vary.

$$K_a(\hat{B}, f) = \frac{w - K_h(\hat{B}) \cdot \hat{B}^2 - Ke \cdot f \cdot \hat{B}^2}{\sqrt{f} \cdot \hat{B}^{1.5}} \tag{24}$$

This method will be referred to as the *Dlala_sep-method*, short for "Dlala separated", as it is the same as the Dlala method, but separated into three components.

6) Steinmetz implementations: The modified Steinmetz equation (equation 2) and the Generalized Steinmetz equation (equation 3) were implemented. These both have the advantage of being simple to implement, only being one component. However, it is difficult to further process this result, and no alterations are performed to include rotational losses in these implementations.

IV. Including rotational losses

As traditional loss separation methods assume alternating flux in the iron loss calculation, advancements to the original methods must be made for rotating machinery.

A review conducted by Guo et.al. in 2008 concluded that "due to the complicated mechanisms (of rotational core losses), it is not practical to develop a model on strong physical background". Therefore, the loss separation method is recommended also for rotational loss, representing each component by factors and dependencies of flux density and frequency[4]. To the author's knowledge, no major advancements have been made after this publication making other methods superior to the loss separation method for practical engineering use.

A. Choice of coordinate system

It is common practise to include rotational losses by using superposition and summing up losses along two orthogonal axes, as in equation 25. Let *a* and *b* be two orthogonal components in a 2D plane perpendicular to the machine axis (crossection of machine). Then the losses can be found as

$$P_{tot} = P_a + P_b \tag{25}$$

Axes a and b can be be in either x- and y-direction (Cartesian coordinates), radial and tangential direction or *major and minor* direction, where the *major* axis is selected through the point of of maximum amplitude in a flux density locus for a full period of time. The minor axis is then perpendicular to the major. This is represented in figure 4. The radial and tangential components, as well as the major and minor components can be found using the mathematical relation stated in equation 26, where ϕ is the angle relative to the x-axis [28].

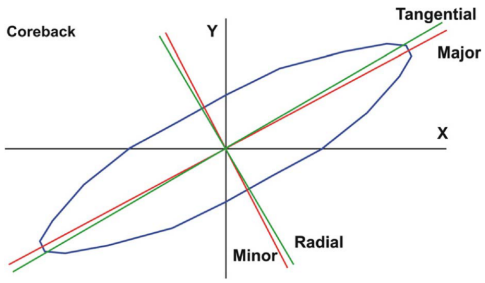

Fig. 4. Representation of different methods for axis decomposition for including rotational losses [28]. The rotating flux is represented as the blue line.

$$\begin{bmatrix} B_a \\ B_b \end{bmatrix} = \begin{bmatrix} cos(\phi) & sin(\phi) \\ sin(\phi) & -cos(\phi) \end{bmatrix} \begin{bmatrix} B_x \\ B_y \end{bmatrix} \tag{26}$$

Finite-element software can often give output in x- and y-direction. However, using the B-field in x-and y-direction has been shown to introduce geometry-dependent inconsistencies [28]. This is related to the anomalous loss component being calculated by the power of 1.5 per axis before summation, thus making the axis contribution significant for the final result. As the eddy current term is calculated to the power of 2, the rotation of axis is not significant, as is the hysteresis term , which is axis independent due to only depending on peak induction [28]. More preferred is using the major/minor method, which has been seen to be more accurate than Cartesian coordinates in several works [28], [36], [5].

Huang et.al. [42] used a three term Bertotti-equation in the frequency domain(eq.6), and decomposed the B-field in major and minor directions. Harmonic analysis was performed, summing opp the losses for each harmonic, each FEM-element, and in major and minor direction. The calculation is performed for a high-speed PM motor with concentrated windings, showing improved accuracy compared to standard FEA calculation(ANSYS built-in) accounting only for alternating loss. However, there is still some discrepancy from measured results, with a maximum error of 15%, however below 10% for rotational speeds below 12 000 rpm. Other examples of losses summed in major and minor direction can be found in [36] [46].

However, the radial/tangential coordinate system has been shown to give quite similar accuracy as the major/minor system. With an average difference of 1 % for calculations in a synchronous generator, and elemental maximum difference of 4 %, the radial/tangential system was recommended as a good engineering compromise in [28], providing over 6 times faster calculation than the major/minor. This is because the major/minor method requires extracting a full loop of data for each element to identify the maximum, followed by post-processing, whereas the radial/tangential method can be applied directly. The similarity in accuracy is explained

by the radial and tangential components often being aligned with radial and tangential axes. In the teeth, the major axis is expected to align with the radial, and in the yoke, the major axis lies along the tangential. The largest discrepancies are thus found in the back corners of the teeth, where the major axis shifts from radial to tangential [28]

B. Rotational loss density

Appino et.al. performed measurements of rotational loss for a Fe-Si steel sheet for the frequency range 2 Hz - 1kHz [48]. It was verified that the rotational losses can be estimated knowing a limited number of measurements for alternating flux, due to a general relationship between rotational and alternating losses. The relation supports the loss separation theory, where different behaviour can be attributed to the the separate loss components, also for rotational loss. This typical relationship is presented in figure 5, which is based on measurements on the Fe-Si steel. The measurements were performed by applying a purely circular flux loci to find W_{rot}, and purely alternating flux to find W_{alt}. It is seen that the rotational losses are expected to be highest at about 75% saturation level, and that the hysteresis component is expected to be clearly dominant. The hysteresis and anomalous (excess) loss component disappear for high polarisation, while the eddy current component has a steady increase. This is explained by the authors to be due to the disappearance of domain walls when purely circular flux loci is applied at saturation level, and claimed to be the first experimental verification of this theory.

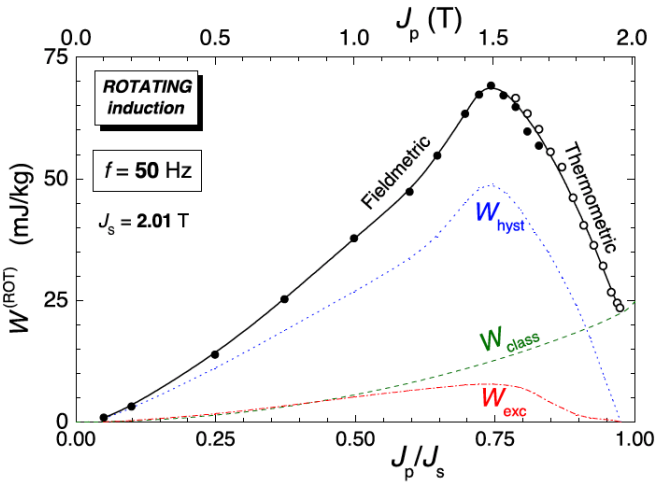

Fig. 5. Rotational loss at 50 Hz [48]. J_p represents the level of polarisation and J_s is the maximum saturation at 2.01 T.

The relation between the alternating and the rotational losses can be represented by a curve *R(Jp)*, which is the ratio $\frac{W_{rot}}{W_{hyst}}$. J_p is the peak polarisation. Such curves are presented for quasi-static hysteresis loss and anomalous loss for the Fe-Si steel in figure 6. This relation is found to be fairly general for non-oriented steels when the skin effect is neglected, which is assumed to valid for frequencies lower than 300 Hz [48].

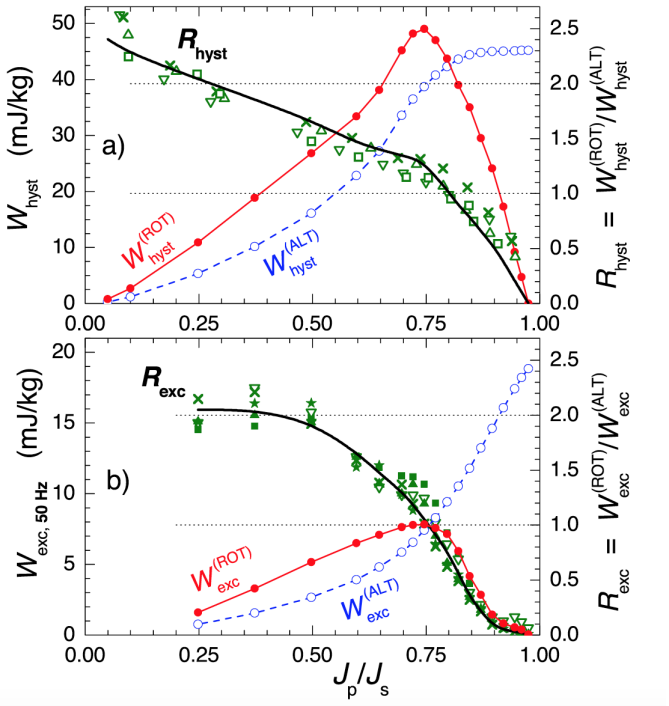

Fig. 6. Rotational loss versus alternating loss presented in [48], measured at frequencies between 20 and 300 Hz.

From the above described results, Appino et. al.[48] concluded that the rotational iron losses can be described by equation 27.

$$W^{ROT}(J_p, f) = R_{hyst}(J_p) \cdot {W_{hyst}}^{ALT}(J_p) + 2 \cdot {W_{eddy}}^{ALT}(J_p, f) + R_{anom}(J_p) \cdot {W_{anom}}^{ALT}(J_p, f) \quad (27)$$

Similar results as presented in figure 5 was found in [49] for investigation of 35 mm lamination non-oriented silicon-iron (SiFe) steel up to 2 kHz. However, in this work the losses were not decomposed by loss separation, but are presented in total.

C. Calculation by use of aspect ratio

To evaluate the degree of rotational flux in the machine, the *aspect ratio* can be used. This is a way to express the relation between pulsating and circular flux in a specific point in the machine. The aspect ratio can be expressed as in equation 28, where B_{min} and B_{max} are respectively the smallest and largest flux density magnitudes during an electrical period, using the fundamental components of the flux density loci [3]. Figure 4 can be used for illustration of this, where B_{max} corresponds to the maximum amplitude along the major axis and B_{min} to the maximum amplitude along the minor axis.

$$\Gamma = \frac{B_{min}}{B_{max}} \quad (28)$$

For purely pulsating flux, B_{min} goes to zero and $\Gamma = 0$. For purely circular flux, $\Gamma = 1$ [3].

Ranlof et.al used the aspect ratio to include rotational losses in studies of twelve large hydro generators [50] . Three methods were compared, where a traditional Bertotti-equation (eq. 6, $\alpha = 2$) was used as a base, and further expanded to include rotational losses by the use of aspect ratio, resulting in equation 29. These two methods were not used with Fourier analysis, i.e. only the fundamental component is included. The increase in loss density due to rotational flux is expressed by the weight factor δ. This could be expressed as a function of $\hat{B}$, but is set to 0.6 in this research due to lack of data.

$$P_{tot_{freq}} = (1+\delta\Gamma)\cdot(K_h\cdot\hat{B}^2\cdot f + K_e\cdot\hat{B}^2\cdot f^2 + K_a\cdot\hat{B}^{1.5}\cdot f^{1.5}) \tag{29}$$

The third expansion calculates in the time domain, thereby including harmonics. This version uses functions $R_h(\hat{B})$ and $R_a(\hat{B})$ to express the rotational loss density relative to the alternating, and are corresponding to the curves presented in figure 6. This model thereby has the ability to address the rotational loss increase per loss component. The model is presented in equation 30.

$$\begin{aligned} &P_{tot_{time}} = \\ &((1-\Gamma) + \Gamma\cdot R_h(\hat{B}))\cdot K_h\cdot\hat{B}^2\cdot f \\ &+ K_e\cdot\frac{1}{2\pi^2}\frac{1}{T}\int_0^T\left|\frac{dB(t)}{dt}\right|^2 dt \\ &+ ((1-\Gamma) + \Gamma\cdot R_a(\hat{B}))\cdot K_a\cdot\frac{1}{8.76}\frac{1}{T}\int_0^T\left|\frac{dB(t)}{dt}\right|^{1.5} dt \end{aligned} \tag{30}$$

It was found that the time domain model (equation 30) predicts 38% higher losses than the traditional Bertotti-model (only alternating), whereas the frequency domain model (equation 29) predicts 13% higher loss than the traditional Bertotti. However, it should be pointed out that the investigation is performed on old machines, complicating the process of finding relevant material data. Therefore, many approximations and assumptions are made to find the correction factors $\delta, R_h(\hat{B})$ and $R_a(\hat{B})$. Another interesting indication from this work is that there seems to be more rotational loss for geometries with short stator teeth for generators with large stators, ie. low flux densities at no load. This finding is supported by [3], who found machines with larger yokes, smaller air gaps and operation point close to saturation to be likely to have a higher percentage of rotational flux, and thereby a higher loss density.

Similar methods to equation 29 is seen in [43], where δ is set to 0.96 due to "iron core manufacture", and in [51], where δ is set to one due to difficulty of determining this value. In [51], Fourier analysis is used and Γ is found per harmonic.

Akiror calculated losses accounting for rotational flux and non-sinusoidal waveforms by use of a rotating loss to pulsating loss ratio *r*, axis decomposition and time dependent expressions for the dynamic losses [3]. The ratio *r* is a function of the aspect ratio and the flux density, and is based on rotational loss measurements. The expression is given in equation 31.

$$\begin{aligned} P^{ROT} = r(\hat{B},\Gamma))[&K_{hx} f\hat{B}^{\alpha x} + K_{dx}\frac{1}{T}\int_0^T\left(\frac{dB_x}{dt}\right)^2 dt \\ &+ K_{hy} f\hat{B}^{\alpha y} + K_{dy}\frac{1}{T}\int_0^T\left(\frac{dB_y}{dt}\right)^2 dt] \end{aligned} \tag{31}$$

The coefficients α, K_h and K_d are corresponding to the constant Jordan/Bertotti coefficients for quasi-static hysteresis and dynamic losses. They are additionally uniquely extracted for x and y-direction. This method produced core loss estimations that were 12-40% higher than losses estimated assuming pulsating sinusoidal flux.

D. Extending the selected methods to include rotational losses

The selected methods described in section III-F were extended to include rotational losses in three steps.

1) Axis decomposition: All methods were extended for orthogonal axes. Radial and tangential components, as well as major and minor components were attempted implemented.

Expressions for the axis decomposition were derived using equation 26 and trigonometric relations. The expression for the radial and tangential components is given in equation 32, where where X and Y are the evaluation point coordinates. The major and minor-expressions are directly derived from equation 26, where the angle ϕ is found using equation 33 evaluated at the time instant t_1 where the flux density magnitude reaches its maximum.

$$\begin{aligned} B_{radial} &= \frac{B_x\cdot X + B_y\cdot Y}{\sqrt{X^2+Y^2}} \\ B_{tangential} &= \frac{B_x\cdot Y - B_y\cdot X}{\sqrt{X^2+Y^2}} \end{aligned} \tag{32}$$

where X and Y are the evaluation coordinates.

$$\phi = \arctan\left(\frac{By}{Bx}\right)\Big|_{t=t_1} \tag{33}$$

2) Aspect ratio and rotational loss density: The model presented in equation 30 was selected for implementation. Implementations using this formula will be referred to with *aspect ratio* in the name. This extension was only possible to perform for the time-dependent models with three components, i.e *Bertotti time* and *Dlala_sep time*.

3) Combination of aspect ratio and radial and tangential components: Equation 30 was combined with using radial and tangential components by replacing the part representing the magnitude of losses per component by the sum of the radial and tangential losses per loss component, as presented in equation 34.

$$
\begin{aligned}
&P_{tot_{time}} = \\
&((1-\Gamma)+\Gamma\cdot R_h(\hat{B}))\cdot K_h\cdot(\hat{B_r}^2+\hat{B_t}^2)\cdot f \\
&+K_e\cdot\frac{1}{2\pi^2}\frac{1}{T}\left(\int_0^T\left|\frac{dB_r(t)}{dt}\right|^2dt+\int_0^T\left|\frac{dB_t(t)}{dt}\right|^2dt\right) \\
&+((1-\Gamma)+\Gamma\cdot R_a(\hat{B}))\cdot K_a\cdot\frac{1}{8.76}\frac{1}{T} \\
&\left(\int_0^T\left|\frac{dB_r(t)}{dt}\right|^{1.5}+\int_0^T\left|\frac{dB_t(t)}{dt}\right|^{1.5}dt\right)
\end{aligned}
\tag{34}
$$

This implementation is recognised by using the names *aspect ratio* and *rad/tan* appended to the model name. The extension was performed for the same models as above, i.e *Bertotti time* and *Dlala_sep time*.

V. Developing a benchmark model

To evaluate the accuracy of the loss calculation methods on common ground, a FEM model was developed. As comparison towards measured results was desired, a machine studied and tested in the doctoral thesis of Erlend Engevik [52] was selected, due to a large amount of measured data both for stator iron loss and machine operating conditions. The machine is a test setup for large hydro power generators built and tested at Uppsala University in Sweden.

A. Machine input data

The machine input data is given in table II. Additionally, the Ansys Maxwell model used by Engevik was made available to further secure exact measurement comparability.

TABLE II
Machine input data given in [52]

Power [kVA]	75
Power factor	0.9
Speed [rpm]	500
Number of poles	12
Number of slots	108
Number of slots per pole and phase	3
Stator outer diameter [m]	0.876
Air gap diameter [m]	0.725
Machine length[m]	0.303.

Measurements of BH curve in the stator and rotor iron where also given. These can be found in appendix A1 and A2.

The winding layout was read of the Ansys Maxwell model and is presented in table III. It is a distributed single layer winding with coil pitch 9. This winding layout is confirmed by Emetor winding calculator [53] to be the layout producing the highest winding factor for a machine with the selected number of poles and slots. The winding factor is 0.96, and there are two turns per slot.

TABLE III
Winding Layout

A+	A+	A+	C-	C-	C-	B+	B+	B+	A-	A-	A-	C+	C+	C+	B-	B-	B-

B. Building the model

A 2D model was made using Comsol Multiphysics 5.4, where rotating magnetic machinery physics was was selected. As the basic winding can be found after 18 slots, a sixth of the machine was modelled. The air gap was split in two domains, where a rotating mesh was applied to two the inner air gap layer and the rotor. A continuous sector symmetry condition was applied at the boundary in the air gap. Continuity boundary conditions were also applied for the sides of the geometry. A force calculation was applied to the rotor. The finalized geometry can be seen in figure 7, where the winding layout is represented by colours.

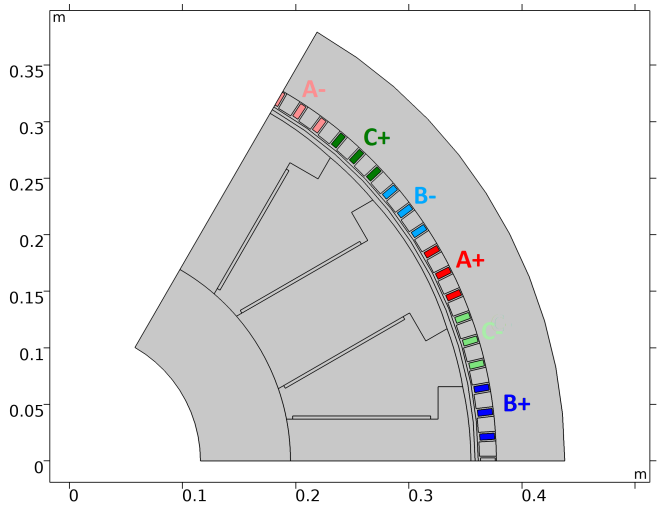

Fig. 7. The geometry built in Comsol with winding implementation represented by colouring

1) Material implementation: The COMSOL built-in materials for air, copper and soft iron (without losses) was loaded and implemented at their respective domains. Copper was laid at the stator windings and the field winding. Two soft-iron materials were defined, one for stator iron and one for rotor iron. The default BH-curves were replaced by the BH curves measured at the test rig at Uppsala University, which can be found in appendix A1 and A2. The default electrical conductivity of zero was used. This is due to the thin laminations largely limiting the eddy currents. As the eddy currents are assumed to create very little opposing field compared to the main field generated by the field windings, the conductivity is not needed for accurate field solution. This is to simplify the model due to high complexity of implementing laminations in 2D geometry. The BH-burve for the stator iron is presented in figure 8.

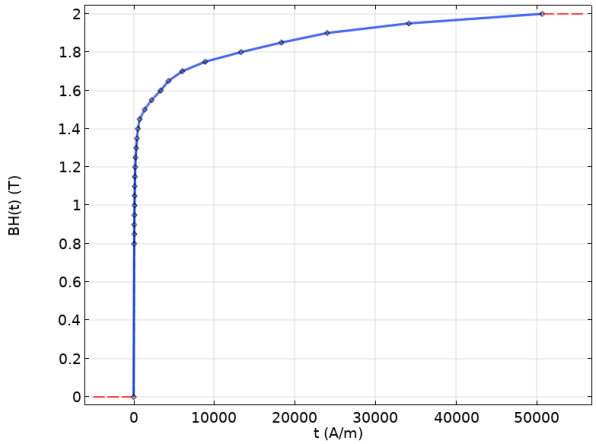

Fig. 8. BH curve implemented in material for stator iron

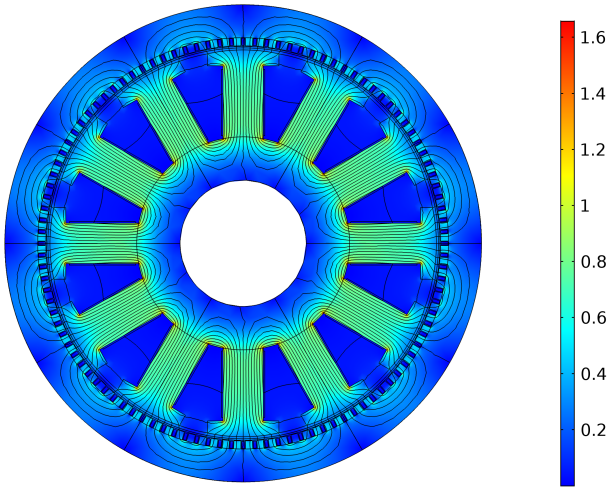

Fig. 10. Flux density distribution in the machine plotted on a 2D grid

2) Mesh selection and solution performance: The mesh was designed to provide sufficiently accurate, but quick solution. The final mesh is shown in figure 9, where a closeup of the meshing in the air gap is given in the upper right corner. The model solves in approximately 2 minutes. The function "copy edge" is used both for copying source to destination in the air gap, and on the outer sides of rotor and stator due to the use of symmetry conditions.

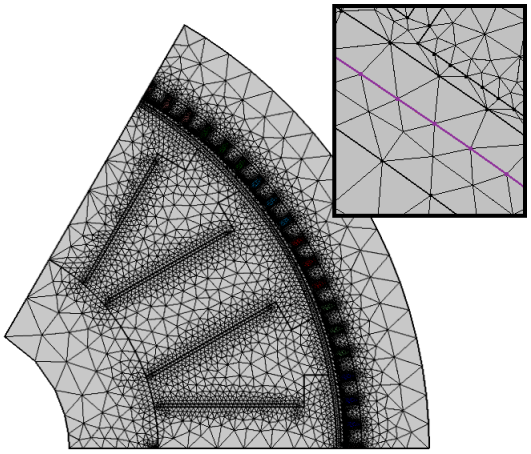

Fig. 9. Mesh used for FEM simulations of the hydro generator

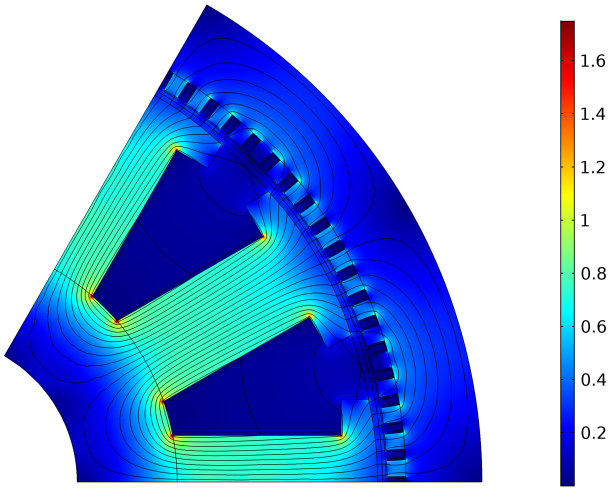

Fig. 11. Flux density distribution on the modelled sector

C. Model verification

To verify the validity of the model, voltage and air gap flux was compared the measured values. Figure 10 presents the flux density distribution in the machine, where the plot is made on a 2D data surface repeating the simulated sector. It is seen that the field lines run as expected and the field looks smooth and continuous, indicating good meshing in the edges and correct use of symmetry conditions. Taking a closer look at the modelled sector in figure 11, it is clear that the overall flux density is low, except some small points in the corners of the poles. The field lines run radially through the poles, as expected.

The phase voltages for nominal field current 12 A are presented in figure 12, verifying the phase voltages are balanced. Furthermore, a comparison of measured and simulated phase voltages for varying field current is presented in figure 13. The phase voltages show very accurate correlation with the measured values. This is a bit surprising as Engevik found the measured voltages to be too low in his Ansys Maxwell-model, and thereby concluded the air gap should be reduced by 0.9 mm to ensure model validity [52]. Engevik modelled the windings as coupled to an external circuit, which might be an explanation for the difference.

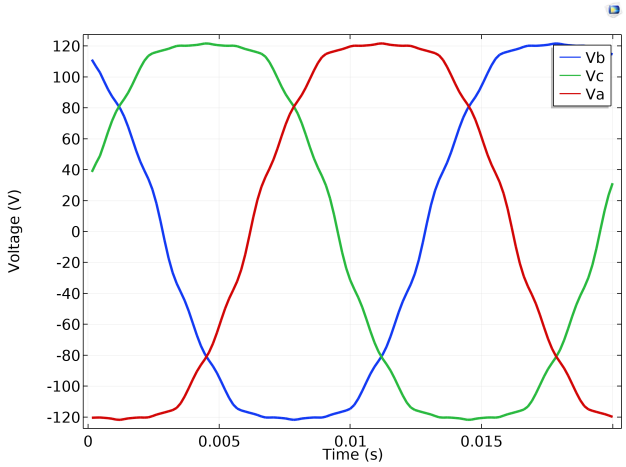

Fig. 12. Phase voltages at field current 12 A (nominal)

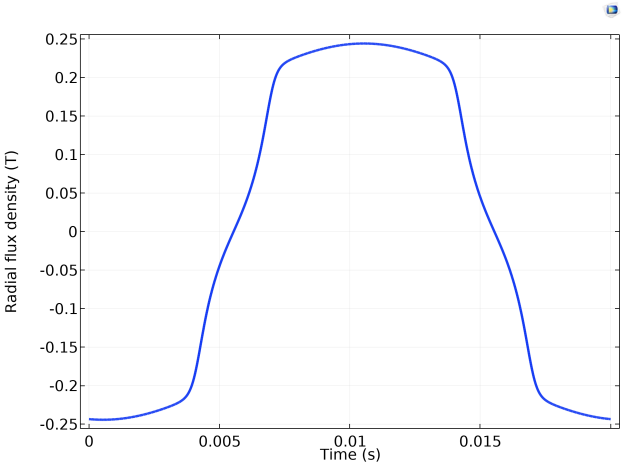

Fig. 14. Air gap flux in radial direction simulated at a point in the middle of a stator tooth at 9 A field current

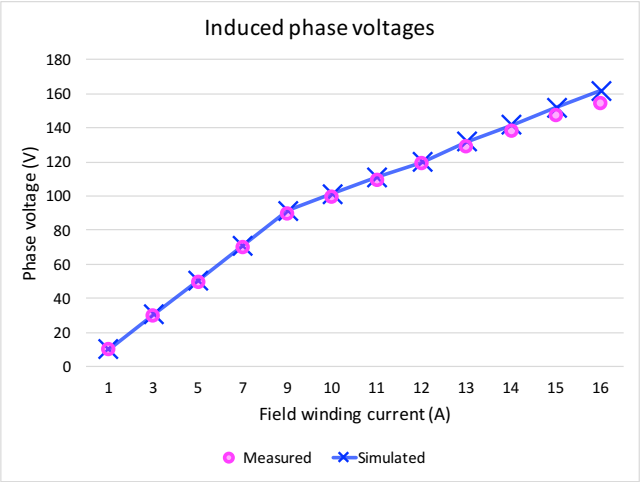

Fig. 13. Phase voltages at field current 12 A (nominal)

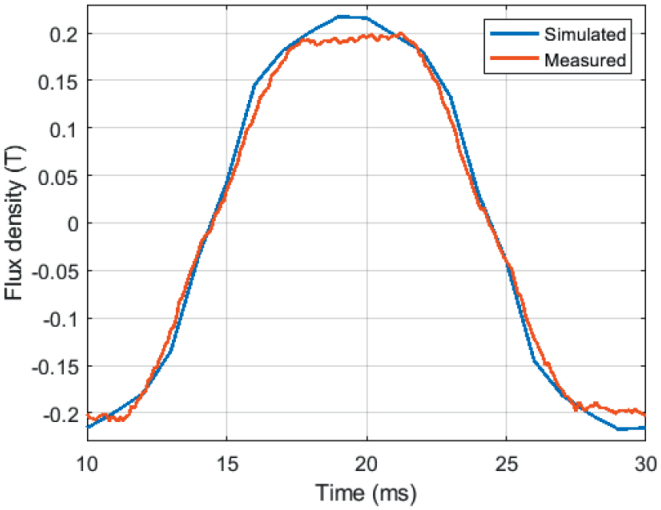

Fig. 15. Air gap flux found by Engevik in [52] at 9 A field current and no-load

The radial air gap flux is presented in figure 14 and compared to the values found by Engevik presented in figure 15 . The simulated values in the COMSOL model are similar to the values found by Engevik using Ansys Maxwell, and correspond well with the measured values. However, the simulated values in the COMSOL model (figure 14) has somewhat higher peak value than the measured values presented in figure 15, with a little under 0.05 T difference.

From these evaluations, the model seems comparable to the measured results. As the flux density has direct impact on the loss calculations, and the voltage is proportional to flux density, these properties are the most important the ensure the model can be used for loss evaluations. However, the slightly high flux density might lead to a small overestimation of losses.

D. Investigation of machine characteristics

A quick investigation of some machine characteristics was performed to evaluate need for advanced loss model extensions. Cut points where set in the geometry to represent the flux variation throughout the stator. The selected points are presented in figure 16.

Plotting of the flux densities in radial and tangential direction is presented in figure 17. The radial components are recognized by the solid lines and the tangential components by the dotted lines. The colours represent the corresponding cut point in the geometry marked in figure 16. It can be seen that the points of highest magnitude in the radial direction are the points in the tooth (points 1,2,3), while the largest tangential components originate from the point just above the slot (point 6). The point furthest out in the yoke (point 7) has a large tangential component and small radial component.

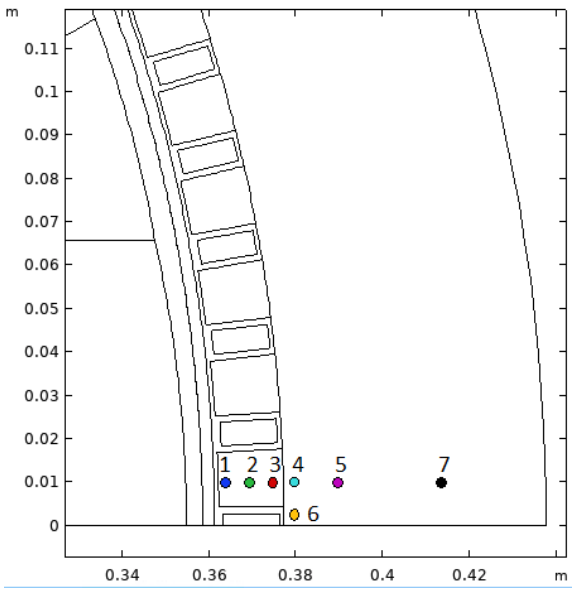

Fig. 16. Measuring points selected in COMSOL to evaluate flux density variations

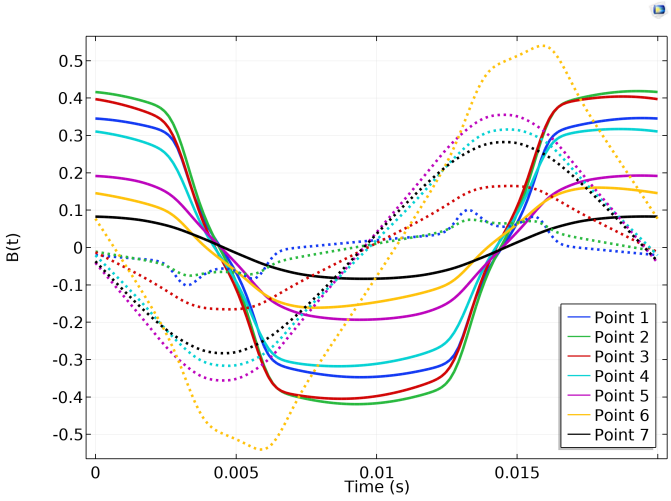

Fig. 17. Radial and tangential flux density components plotted for the selected points marked in figure 16. The tangential components are marked by dotted lines

Figure 18 shows the existence of flux density harmonics in the machine. The plot is generated using the built in function *Transformation* and selecting *Frequency spectrum* in the plot settings. The Fourier transform shows the fundamental (50 Hz) is clearly dominant for all the points. However, third harmonics (150 Hz) are also apparent, particularly in the teeth. A small degree of seventh (350 Hz) and ninth (450 Hz) harmonics can also be seen.

In figure 19, the flux loci in the evaluated points are presented, showing very clear existence of rotational flux. The plot is generated by evaluating the radial and tangential components in the selected points and plotting them against each other. As expected from theory, the degree of rotation is highest in the inner parts of the yoke, which is a zone where the flux transitions from flowing close to purely radially to purely tangentially.

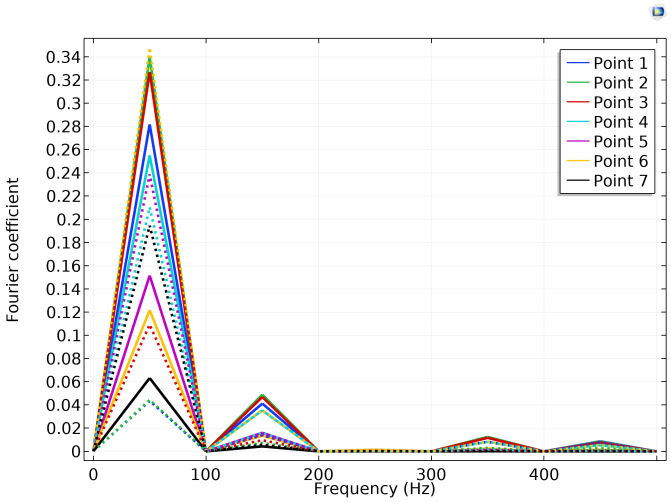

Fig. 18. Fourier transformed flux densities in the measuring points. Tangential components are marked by the dotted lines

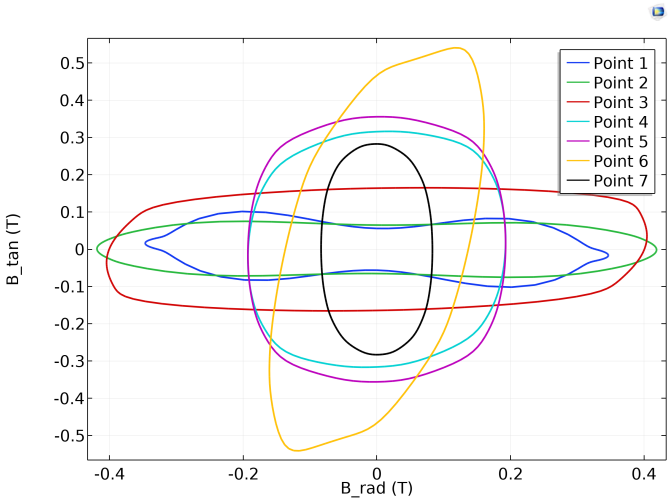

Fig. 19. Flux locus in the measuring points. A high degree of rotation is observed, particularly for the points in the yoke.

From the quick above estimations, it is concluded that the fundamental frequency is expected to be the main source of loss. However, harmonics should be accounted for. Rotational loss must be included.

VI. Implementation of Loss Calculation Methods in COMSOL

A. Coefficient determination

The coefficients were determined using MATLAB and imported to COMSOL to the *parameters* list, which can be found in appendix B3.

Due to the material in the test setup machine being unknown, a material was selected in the doctorate by Engevik to be the best fit compared to his measurements of specific loss

at 50 Hz. This material is SURA M530-50A, and is given in appendix A4. Not knowing exact material specifications is a known problem for older hydro generators.

1) Constant coefficients: The constant coefficients used in Jordan's equation, Bertotti's equation and Steinmetz' equation were determined using "custom equation" in MATLAB Curve fitting tool. The material data from the data sheet was imported to MATLAB as column vectors and thus made available to the curve fitting tool. By studying the coefficients generated by the built in core loss function in Ansys Maxwell for the model by Engevik, it was concluded that these were found using only the 50 Hz frequencies. As using only the 50Hz values seemed to give the most probable coefficients for this case as well, these were selected for the Bertotti-coefficient. However, for the Jordan coefficients, this was not sufficient data, as coefficients were completely dependent on the bounds that were adjusted manually. Therefore, loss data from 50 Hz to 400 Hz was used to find the Jordan coefficients, which gave a much more robust fit. This data was also used for the Steinmetz fit. The classical eddy current coefficient for the Bertotti method was calculated analytically using equation 5. The resulting coefficients are presented in IV.

TABLE IV
CONSTANT COEFFICIENTS FOUND BY MATLAB CURVE FITTING TOOL

Method	Coefficent	Value
Jordan	K_h	0,03197
Jordan	K_d	1,96E-04
Bertotti	K_h	0,03278
Bertotti	K_e	1,61E-05
Bertotti	K_a	0,00205
Steinmetz	C_{se}	0,00302
Steinmetz	α	1,592
Steinmetz	β	2,213

2) CAL2: The coefficients for the CAL2-polynomials were found by inserting the polynomial equations (20) into the linear loss ratio formula (13), and inserting this expression into the MATLAB Curve fitting tool. As the material data provided specific loss for 50 Hz, 100 Hz, 200 Hz and 400 Hz, which are closely related to the observed harmonics at 150 Hz, 350 Hz and 450 Hz, all frequencies were used for the polynomial fitting. Thereby, the polynomial fit is based on similar input as the to the low-frequency-fit found by Ionel et.al.[44], which is the only fit needed for this application (as converter harmonics are not included and higher harmonics have not been observed). The hysteresis coefficient k_{h0} was limited by a lower bound of zero, as negative values would indicate negative static energy losses which has no physical basis.

The polynomial coefficients were loaded to the *parameters* list in COMSOL and an analytical function was defined under the component section for each polynomial $K_f(f,\hat{B})$ and $K_c(f,\hat{B})$ (using equations 20a, 20b). The input data to the polynomial was set to be of unit T and the output of unit J/T^2. The input range of B was limited to $[0,2]$. An example implementation is given in appendix B5.

3) Dlala: The coefficients for the Dlala method were found by the scripting the methodology described in section III-F.4 in MATLAB. The input data was divided into column vectors per flux density and a linear curve fit was made for each vector, as presented in figure 20. Frequencies 50 Hz, 100 Hz, 200 Hz and 400 Hz were used, but only flux densities from 0.2T to 1.5 T could be used, as equal amount of frequency levels per flux density was needed for the linear fit. Thereby, flux densities 1.6 T and 1.8 T at 50 Hz is left out, which was included in the CAL2-fit.

The $K_h(\hat{B})$ coefficients were then read out of the linear fit by setting the frequency to zero (eq. 21) and tabulated. Then $K_c(f,\hat{B})$ was found using formula 22. The scripts write the tabulated coefficients to files, which can be directly imported to COMSOL. An interpolation entry was defined for each set of coefficients ($K_h(\hat{B})$, $K_c(50\,Hz,\hat{B})$, $K_c(100\,Hz,\hat{B})$, $K_c(200\,Hz,\hat{B})$, $K_c(400\,Hz,\hat{B})$), and the corresponding file was imported to each interpolation. The interpolation settings were set to *Cubic spline* and the extrapolation to *Constant*. An example of the COMSOL implementation can be found in appendix B6.

It is seen in the linear fittings presented in figure 20 that the fit is less accurate for the lower flux densities. Knowing that the flux densities are generally low in the intended machine, this is a source of inaccuracy. Moreover it is seen that particularly the low frequencies (50 Hz and 100 Hz) are far from the linear fit for these flux densities. As the lower frequencies are dominant in this machine, this is another disadvantage of this coefficient estimation. Using weight factors to weigh the 50 Hz values more than the others might have been an interesting option. However, due to time limitation and the lack of documentation for such methods, this was not prioritized.

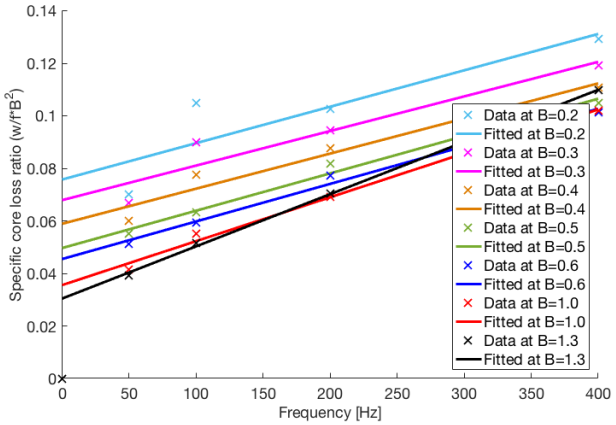

Fig. 20. Linear fit of loss density ratio using method presented in [45]. The linear fit is more accurate for higher flux densities

The resulting fittings of $K_d(f,\hat{B})$ are presented in figure 21. The 50 Hz-fit of $K_d(f,\hat{B})$ is negative for low flux densities, indicating an overestimation of $K_h(\hat{B})$ for these flux densities. This result could be expected from studying

the linear fit in figure 20, where the linear fit lies above the measured value at low flux densities for 50 Hz. Moreover, the high values for $K_d(100\ Hz)$ at low flux densities fits with the linear fit lying low below the measured values. For higher frequencies the fits seem to converge more in value. However, it is interesting that the higher frequencies seem to have higher eddy current coefficients than the 50-Hz fit.

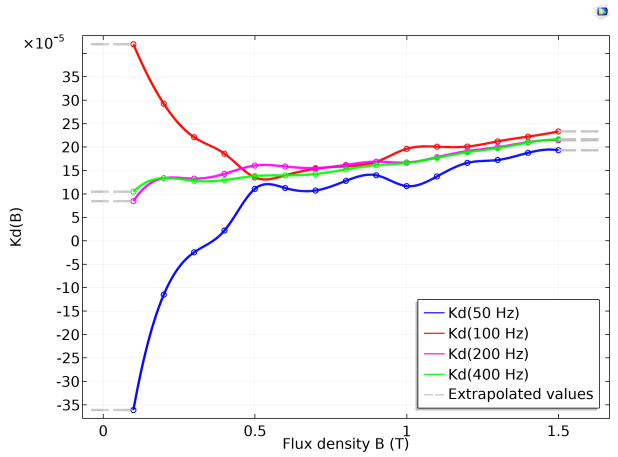

Fig. 21. Plot of variable coefficients using method presented in [45]

As it was found in the literature review that higher frequencies might dominate the solution, the effect of reducing the input data to three frequency levels (50 Hz, 100 Hz, 200 Hz) was compared. The new linear fit can be found in appendix B7. Figure 22 shows a comparison of the $K_h(\hat{B})$ and $K_d(\hat{B}, 50\ Hz)$ for the two different fits. The hysteresis coefficient is slightly reduced, and the classical loss coefficient thereby increased. For the new fit, only $K_d(0.1\,T)$ and $K_d(0.2\ T)$ were slightly negative, whereas for the first fit, also $K_d(0.3\ T)$ was negative. As the negative values have no physical meaning, the fit with the least negative values was selected. It was considered to set the negative values to zero, but this was not done as manual alterations reduce the transparency of the method.

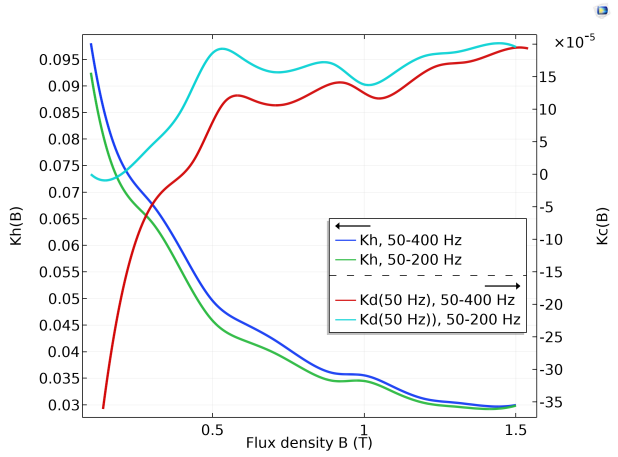

Fig. 22. Comparison of using three versus four levels of frequency for the coefficient approximation for the Dlala method

4) Dlala_sep method: For the *Dlala_sep* method, similar methodology was used as described for the Dlala-method. However, as linear fitting could no longer be used, the fittings per flux density were performed using MATLAB Curve Fitting Tool by inserting equation 23 into the "custom equation"-field. An example of the resulting fit is presented in figure 23. Reading off the values for $K_h(\hat{B})$ at zero frequency and tabulating these, $K_a(\hat{B}, f)$ was found by inserting the tabulated $K_h(\hat{B})$ and the analytically calculated K_e (equation 5) into equation 24, using a modified version of the original Dlala-script. The tabulated values were written to files and imported to COMSOL interpolation entries. Frequencies 50 Hz - 400 Hz was used for this fit. No negative values were obtained.

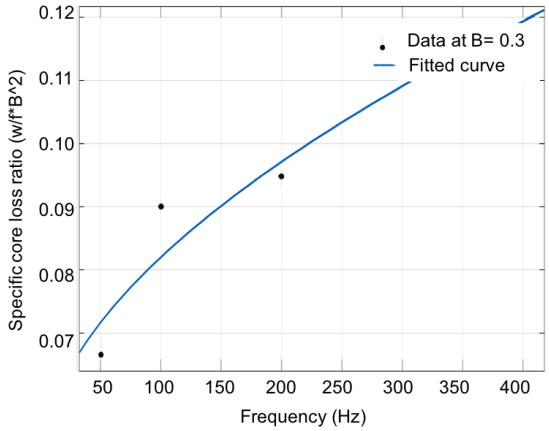

Fig. 23. Fit at 0.3 T using the Dlala_sep method

5) Comparison of methods: A comparison of the resulting coefficients are presented in figures 24, 25 and 26. It is seen that for the hysteresis coefficients (figure 24), the CAL2-coefficient is generally much higher than the others. The coefficient fitted using the Dlala method is much higher than the constant coefficient for low flux densities, but converges towards the constant value for higher flux densities. The Dlala_sep coefficient is somewhat lower than the Dlala coefficent, and drops below the constant hysteresis coefficient for higher flux densities. This seems to be the variable coefficient where the average is closest to the constant coefficient. The Jordan and the Bertotti hysteresis coefficients were so similar they are only represented by one line. It is interesting to note that the CAL2-coefficient and the Dlala-coefficient have very similar value for the first point of flux density (0.2 T), but then develops in completely different manner for increasing flux.

Figure 25 shows the dynamic loss coefficients and the classical eddy current coefficient, determined analytically by equation 5. The constant Jordan-coefficient seems to be close to an averaged value of the CAL2 coefficient. The Dlala coefficient is slightly negative for low flux densities, but increases quickly and reaches the value of the Jordan coefficient at about 0.5 T, thereafter fluctuating around a

value slightly lower than the constant Jordan-coefficient. This correlates with the Dlala-method taking higher values than the Jordan-method for the hysteresis coefficient at low flux densities, and lower values for the dynamic coefficient at low flux densities. This is related to the method used, as dynamic losses are found by subtracting the hysteresis losses (equation 22). However, this trend is also seen in the CAL2-model for low flux densities, whereas for the high flux densities, both hysteresis and dynamic coefficients shoots off to very high values, indicating very large increase in loss prediction relative to the Jordan method for high flux densities. The classical eddy current coefficient K_e is much lower than the others, but of the same order of magnitude.

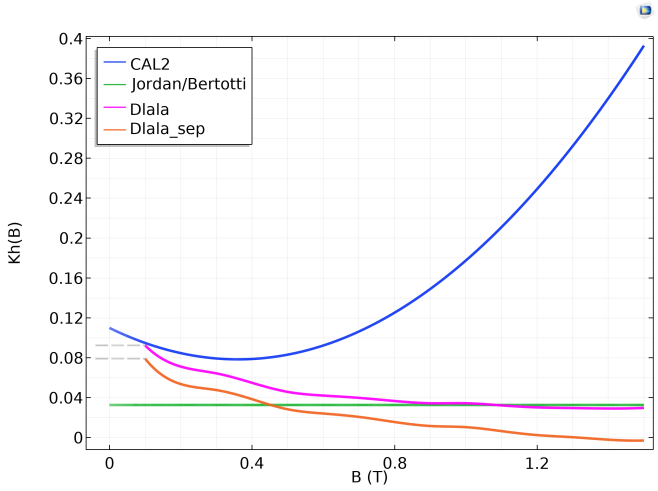

Fig. 24. Comparison of the hysteresis loss coefficients obtained using the selected methods

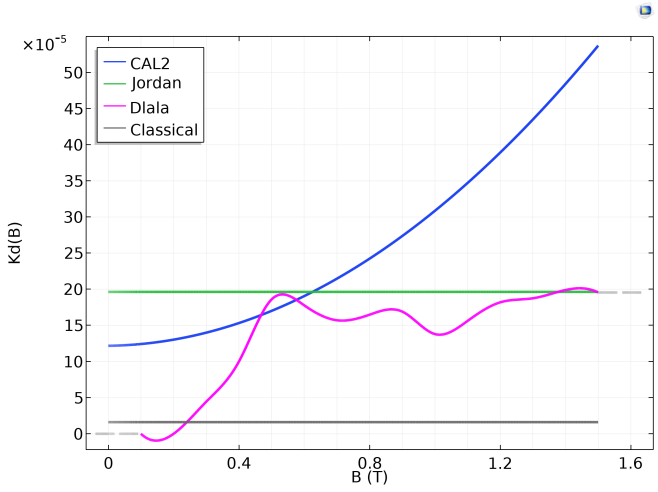

Fig. 25. Comparison of the dynamic loss coefficients obtained using the selected methods

Comparing the anomalous coefficients in figure 26, it is seen that the Dlala_sep-method generates a coefficient increasing quickly from zero to a value about three times higher than the constant Bertotti-coefficient. This correlates to the trend seen for the dynamic loss coefficients, which also seem to increase for increasing flux densities, compensating for the decrease in hysteresis coefficient seen in figure 24. The magnitude of the Dlala_sep anomalous loss-coefficient is much larger than the the eddy current coefficient and the Dlala dynamic loss coefficient in figure 25.

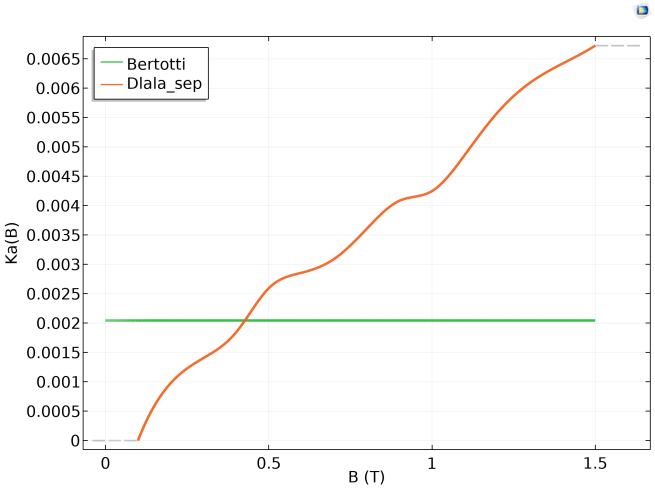

Fig. 26. Comparison of anomalous loss coefficients obtained using Bertotti's method and the Dlala_sep method

B. Implementation by surface integration

All methods are implemented using the *Surface integration*-function in COMSOL. This is found under *Results* -> *Dervied values* -> *Integrations*, and is a method for post processing the field solutions. This means the model only needs to be solved once before results can be extracted. The general expressions for much used functionalities are presented in table V. An example implemtation of evaluations in the surface integration entry can be found in appendix B8. The expressions for evaluation were learned from the COMSOL User Guide [54] and the COMSOL Reference Manual [55] . Much used expressions, like for example to find the peak value of B, was defined as a local variable to ease implementation. A list of the local variables can be found in appendix B4.

The built in size *rmm.normB* was used to represent the flux density. This is the magnitude of the flux density (not a vector) and is found as $\sqrt{{B_x}^2 + {B_y}^2}$ [55].

TABLE V
EVALUATIONS MUCH USED IN COMSOL

Evaluation form	Expression	Example of use
Time derivative	d(exp, inc.)	Finding $\frac{dB}{dt}$
Max.over time	timemax(t1,t2,exp)	Finding B
Time integral	timeint(t1,t2,exp)	Integrating $\frac{dB}{dt}$

It was learned that when using expressions for evaluating over time (*timemax*, *timemin*, *timeint*), the evaluation is performed for every timestep. As each evaluation needs

evaluation of a full time period of data, this seemed to result in outputting the same evaluation for every timestep, as seen in figure 27. This was very slow. To avoid this, the *Time selection* under *Surface integration* was set to only one arbitrary time step. For all evaluations in this thesis, this was set to *first*. The validity of this method was checked for several loss calculations, and output can be found in appendix B9. The time saved by doing this was extreme. For advanced inputs with a large degree of expressions (like for example CAL2 time dependent formula implementation), the time evaluation of a single surface integration was reduced from approximately 15 hours to 3 minutes.

timemax(0,T,rmm.normB)	timeint(0,T,rmm.normB,'n
0.010690	0.0046089
0.010690	0.0046089
0.010690	0.0046089
0.010690	0.0046089
0.010690	0.0046089
0.010690	0.0046089
0.010690	0.0046089
0.010690	0.0046089
0.010690	0.0046089
0.010690	0.0046089
0.010690	0.0046089
0.010690	0.0046089

Fig. 27. Example of COMSOL outputting the same result for all time steps inducing extremely high computational time

C. Implementation of rotational loss models

1) Axes decomposition: The expressions for radial, tangential, major and minor flux density components were defined as local variables in COMSOL, and the explicit expressions can be found in the appendix B4.

The time instant t_1 used for finding the angle ϕ in equation 33 is at the point where *normB* reaches its max. The angle ϕ was found using the built in *attimemax()* function, and the full expression is found in the variables-list in appendix B4.

The losses were calculated relative to the separate axes according to equation 25 by using the already implemented methods and replacing the *rmm.normB* with the relevant B-vector. However, COMSOL would not evaluate the B_{major} and B_{minor} expressions using *timemax(),timeint()* functions. The reason for this is unknown to this author, as plotting over time was possible, likewise differentiation. As it was thereby not possible to use the implemented methods with the major and minor axes, no more work was performed on this area. However, it might have been interesting to perform such analysis to compare with the results for radial and tangential components.

To evaluate the expected discrepancy of using radial and tangential components compared to using major and minor, the flux loci using major and minor axes is presented in figure 28. Comparing this to figure 19 showing flux loci using radial and tangential components, some differences can be noted. The flux loci in the teeth (points 1,2,3) are very similar, as the major axis lies along the radial axis. For the points further out in the yoke (points 5 and 7), the loci has been shifted 90 degrees, aligning the tangential axis with the major axis. The largest difference is seen in the points just behind the tooth (point 4) and just behind the slot (point 6). Point 4 seems to have been rotated 45 degrees, as the major axis lies between the radial and tangential. The flux loci in point 6 has been rotated about 65 degrees in negative direction, so that the corner points lie along the major axis. This shows the axis decomposition is in line with what was found in [28], where major and minor axes aligns with radial and tangential axes for most parts of the machine. The points expected to induce largest discrepancies are the points just behind the teeth, here exemplified by point 4 and 6. As this was shown to have little overall impact in [28], using radial and tangential components is expected to provide acceptable accuracy for this analysis.

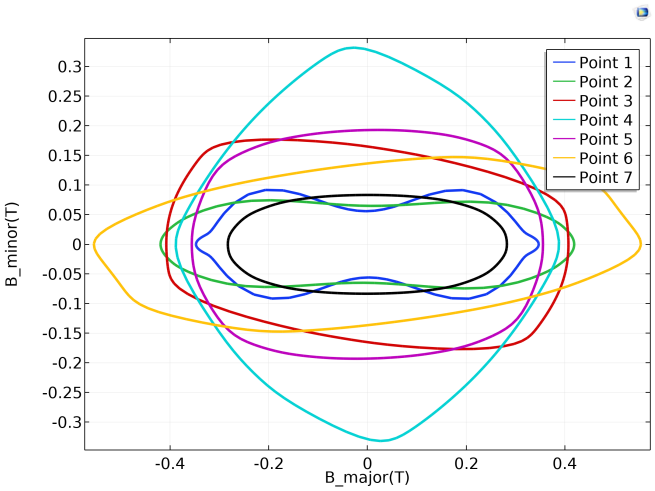

Fig. 28. Flux loci decomposed in major and minor axes

2) Aspect ratio and rotational loss density: The data for the R-curves (ratio of rotational loss density relative to alternating loss) needed for equation 30 was extracted from the work presented by Appino et.al. [48] using MATLAB GRABIT[56]. This data was selected as it was claimed to be generic for non-oriented steels when skin effect is neglected [48]. The extracted data was imported to COMSOL as an interpolation-entry with linear interpolation and constant extrapolation, as shown in appendix B10. For running the model in COMSOL, the flux density B is used as input to the model in stead of the polarisation P. This might be a source of inaccuracy, but is expected to be a valid simplification, knowing flux densities are low.

The aspect ratio plotted over the surface of the machine is presented in figure 29. This shows the level of rotation is indeed existent, as expected from the results in the model investigation (section V-D).

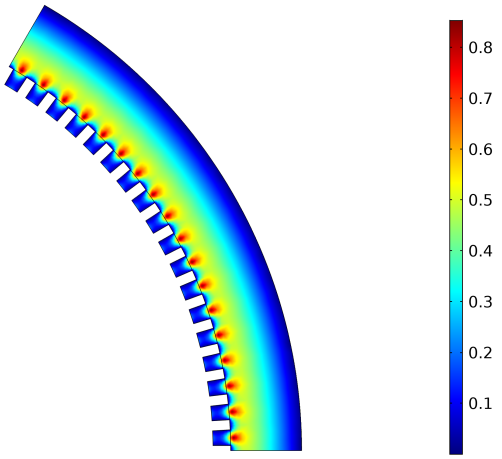

Fig. 29. Aspect ratio Bmin/Bmax for 12 A field current. 0 indicates purely alternating, 1 indicates purely circular flux loci

VII. Modelling Results

The losses were calculated varying the field current between 3 A and 16 A and compared to the values measured by Engevik in [52].

A. Comparison of methods excluding rotation

The losses calculated using *normB* to represent the flux density are presented in figure 30. It is seen that the CAL2-model, both fundamental and time domain, lies close to the measured value until the field current reaches 12 A, where it shoots into an overestimation. The GSE, on the other hand, generally grossly underestimates losses, and is therefore not further discussed in this section. Overall, the frequency-domain models seem to be more accurate than their corresponding time-domain method. This is surprising, as the time domain extension was indented to include harmonics. However, the difference is small, much due to the hysteresis component using the fundamental frequency in both methods and generally being the dominant component. The MSE is also surprisingly accurate, considering its simplicity. For field current higher than 11 A, this is the most accurate method except from CAL2. The two Dlala-implementations and the Bertotti-methods are overlapping and will be further investigated. The Two Jordan-implementations are least accurate, apart from the GSE.

To better evaluate the accuracy of the calculations, a correction factor is defined in equation 35. This factor is the relation between the measured loss and the calculated loss. This kind of factor is often used in loss calculation literature, often to make the values fit to the measured value. In this discussion, k will be referred to as the *needed correction factor*. If k is close to one, the estimation is very accurate. A k higher than one means losses are underestimated, a k lower than one means losses are overestimated.

$$k = \frac{P_{measured}}{P_{calculated}} \tag{35}$$

Figure 31 presents this correction factor for the different methods per field current. In this plot the difference betweeen time- and frequency domain models is even more apparent. It is also seen that the accuracy drastically decreases for all methods for low field winding current.

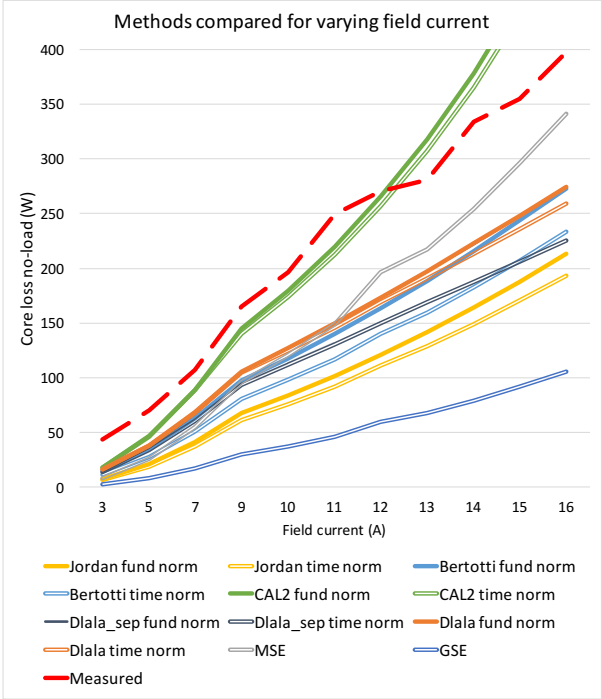

Fig. 30. Loss calculations per variation of field current for the different methods. The red dashed line indicates the measured values.

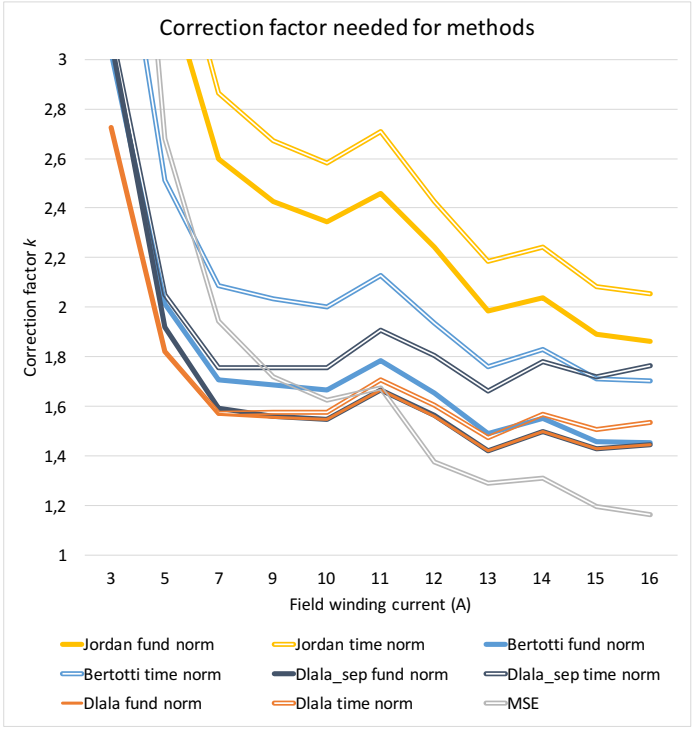

Fig. 31. Needed correction factors for the different methods per field current. The GSE and CAL2 are left out if this plot due to respectively very large needed correction factor and negative correction factor

B. Effect of decomposition to radial and tangential components

The resulting loss calculations when radial and tangential components are used is presented in figure 32. It is seen that the CAL2-methods are very accurate for 9-11 A field current, then shoots into overestimation. This could be expected from the loss coefficient fittings, where both K_h and K_c increase for higher flux densities (figures 24 and 25).

The increase in loss prediction when using radial and tangential components relative to using *normB* is presented in figure 33, showing all results increased significantly. The time-dependent models are more impacted than the fundamental ones, with 11-48% increase compared to 6-17% increase. Particularly the Bertotti-model in the time domain was extremely affected by this, with 37-48 % increase.

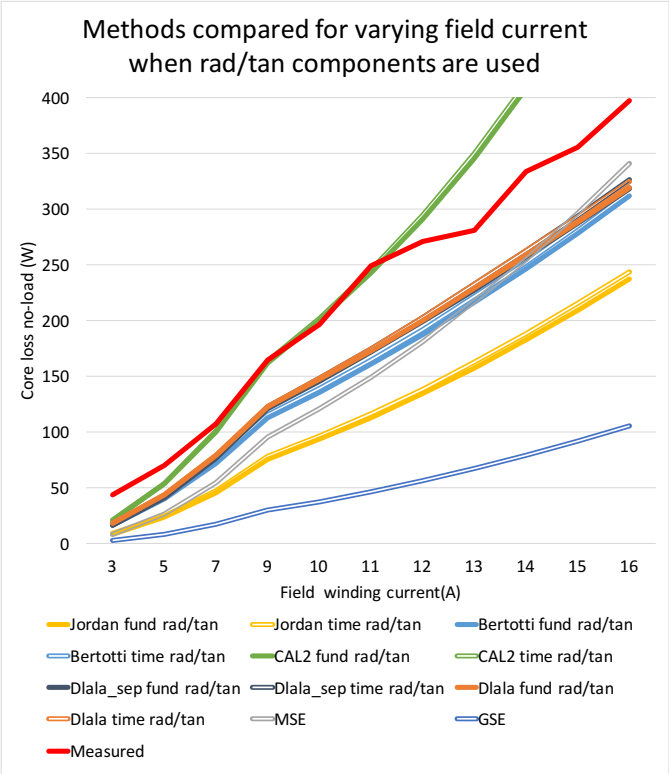

Fig. 32. Loss calculations per variation of field current for the different methods when radial and tangential compoenents are used in calculation. The red dashed line indicates the measured values.

The new *needed correction factors* are presented in figure 34. The difference between the time-dependent and the fundamental models is altered, where the time-dependent models are now slightly more accurate. The general accuracy is also overall increased, where the fundamental models seem to have reduced the needed correction factors by approximately 0.2. Radial and tangential components are not used for the MSE, and it is noted that this method is no longer superior. It can also be noted that the two Dlala-implementations have very similar accuracy, indicating that the change from two components to three components has little impact. However, the trend of increasing accuracy for

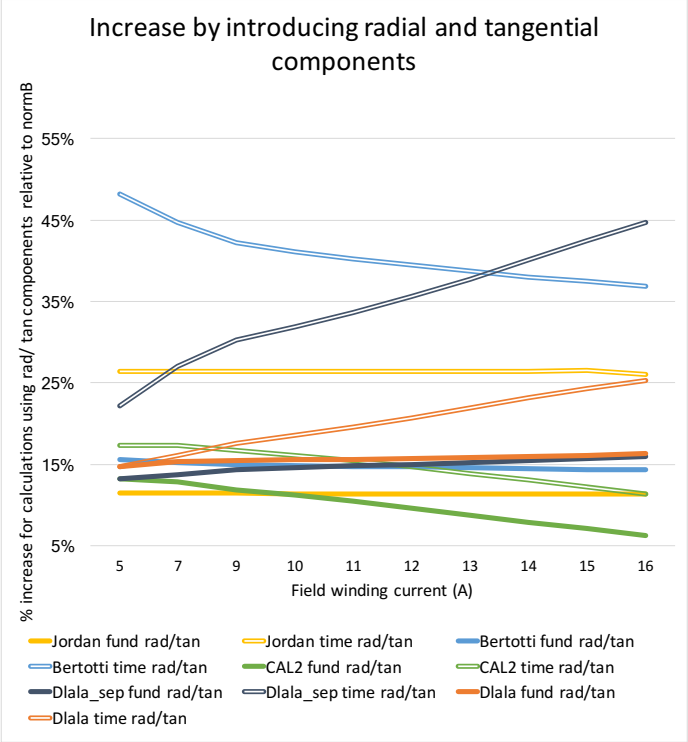

Fig. 33. Increase when radial and tangential components were used, relative to the calculation using normB

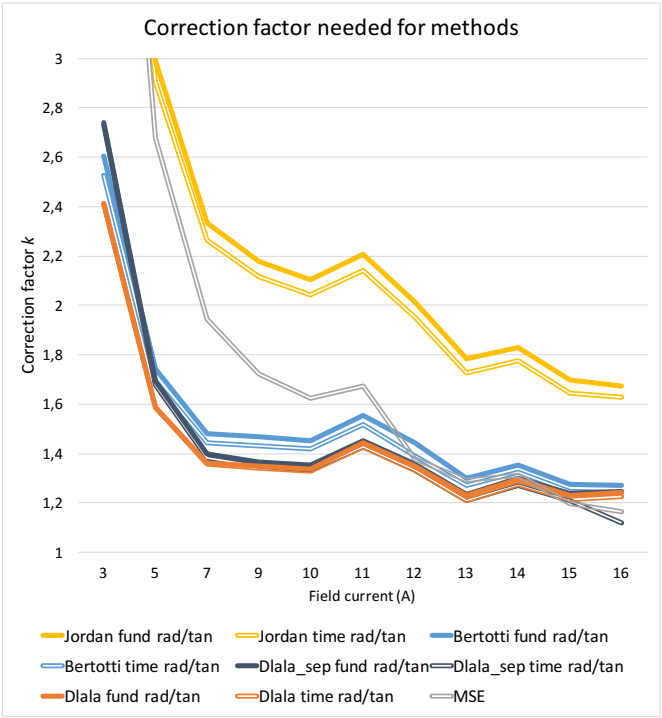

Fig. 34. Needed correction factors for the different methods per field current when radial and tangential components are used. The GSE and CAL to are not presented to improve visibility

higher field current is the same, and overall all methods except the CAL2 generally underestimate the losses.

C. Effect of using the aspect ratio and the rotational loss density

The effect of extending the Bertotti and the Dlala_sep methods to include rotational loss density by the use of aspect ratio is presented in figure 35. The calculations using only radial and tangential components are more accurate than using the aspect ratio and the rotational loss density in combination with *normB*. However, the clearly most accurate method is the combination of the two, which shows good correlation with the measured results for both Bertotti and Dlala_sep. The latter is however slightly more accurate. The accuracy is lowest for the low values of field current.

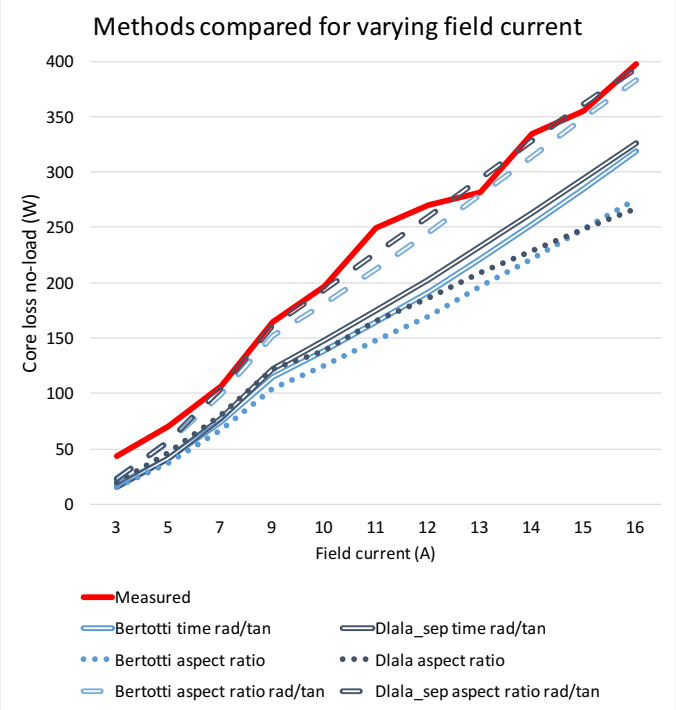

Fig. 35. Comparison between variations of the dime domain versions of Bertotti and Dlala_sep

Figures 36 and 37 show the separated components for the Bertotti and the Dlala_sep methods calculated using both orthogonal components and aspect ratio. Both methods have a share of rotational losses close to 50%. Moreover, the overall component contributions are similar for the two methods. However, differences can be noted for increased field current (increased flux density in the material). At low field current, the hysteresis losses are completely dominant for the Dlala_sep method, whereas the separation between hysteresis and anomalous components are more even for the Bertotti method, somewhat dominated by the anomalous component. Further, as the field current increases, the hysteresis losses in the Dlala_sep methods show a tendency towards flattening out, whereas the hysteresis losses in the Bertotti-method seems to continue increasing drastically. Likewise, the anomalous component in the Dlala_sep method increases as the hysteresis decreases, thereby leaving the total sum of losses fairly similar for the two methods. The implementation of variable coefficients therefore seems to have little effect for evaluating the sum of losses looking at these graphs, however might be important if separation of components is wanted. It is difficult to conclude from this if the variability of the coefficients would have impacted the total sum differently for higher levels of flux density in the material and for a higher degree of harmonics.

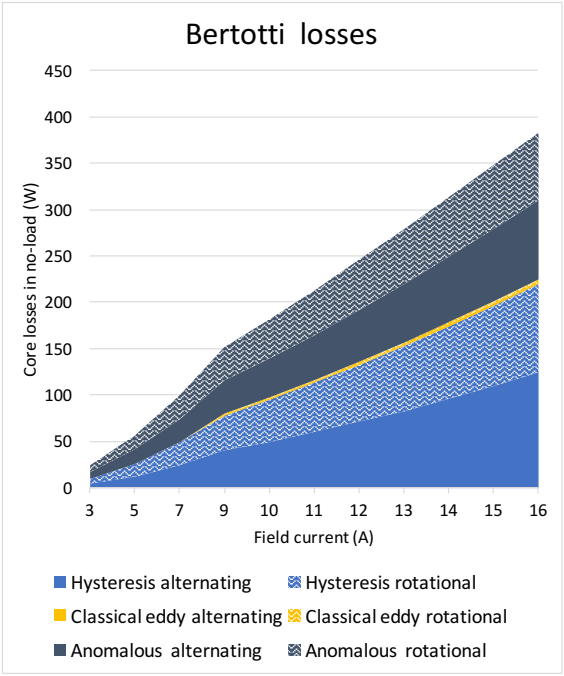

Fig. 36. Components per field current for alternating and rotational field for the Bertotti method

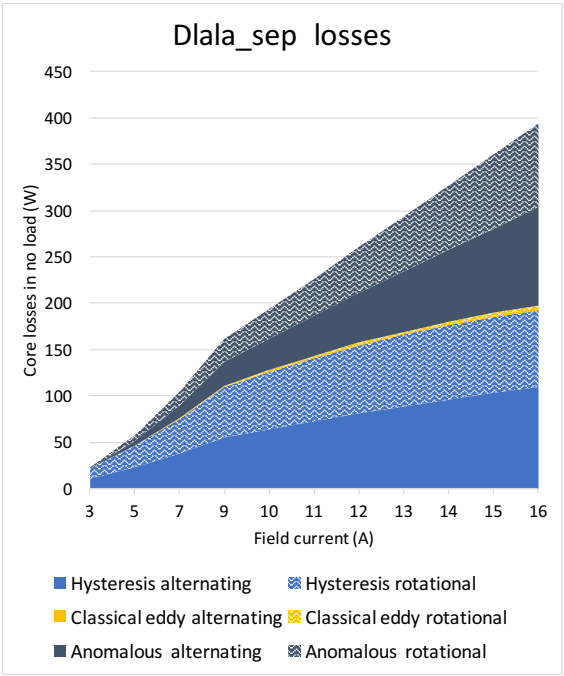

Fig. 37. Components per field current for alternating and rotational field for the Dlala_sep method

D. Overall comparison of methods

The relative error was calculated as $\frac{P_{calculated}-P_{measured}}{P_{measured}}$. The average relative error for calculations using radial and tangential components (except for MSE and GSE) is presented in table VI, showing the CAL2-model had lowest average error. It is also the only model where this value is positive (overestimation). The Dlala_sep model including the aspect ratio also has low relative error with 7% underestimation. Overall the relative error for time domain models are 1-2% lower than the corresponding fundamental frequency-model. If the losses calculated at 3 and 5 A field current are excluded from the averaging, the Dlala_sep method using aspect ratio has an average error of -2% and the Bertotti using aspect ratio has an average error -7%.

TABLE VI
AVERAGE RELATIVE ERROR FOR METHODS USING RADIAL AND TANGENTIAL COMPONENTS

Method	Fund.	Time	Aspect ratio
Jordan	-53 %	-52 %	
Bertotti	-33 %	-31 %	-11 %
CAL2	4 %	5 %	
Dlala	-28 %	-27 %	
Dlala_sep	-29 %	-28 %	-7 %
MSE		-38 %	
GSE		-81 %	

The equivalent frequency used in the MSE was also evaluated separately to verify the method, and was found to be 221,31 Hz at 11 A field winding current and 224.83 Hz for 13 A current.

To estimate the contribution of losses originating from harmonics, the relative difference between the time domain models and the corresponding frequency domain model was investigated. This is presented in figure 38. I can be seen that the contribution from the harmonics lies between 0-3.2% for all methods.

For the variable coefficient-methods, an increase in the contribution from harmonics can be seen for increasing field current in figure 38. This can be related to the separation of components, where a higher degree of dynamic components are seen for increasing field current (related to the increasing dynamic coefficients in figures 25 and 26). Thus, a higher degree of dynamic components can also lead to higher degree of harmonics.

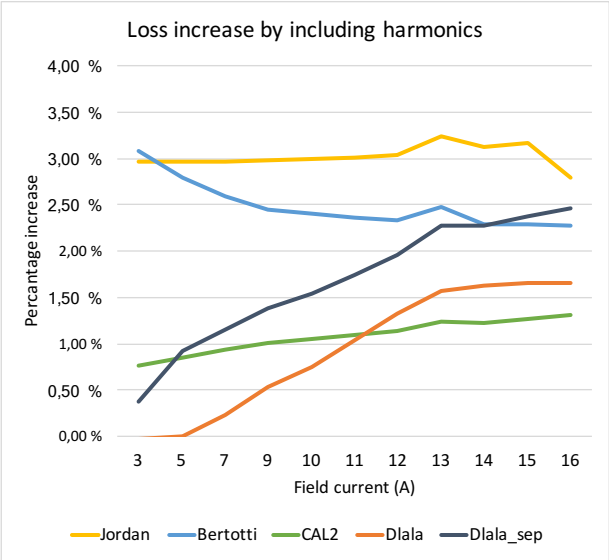

Fig. 38. Increase of losses by including harmonics

E. Comparison of methods for 12 A field winding current

To better understand the loss estimations, a more thorough study is performed for one selected field current. In this section, the properties calculated for 12 A field current is presented. Figure 39 presents the calculated losses for all method variations.

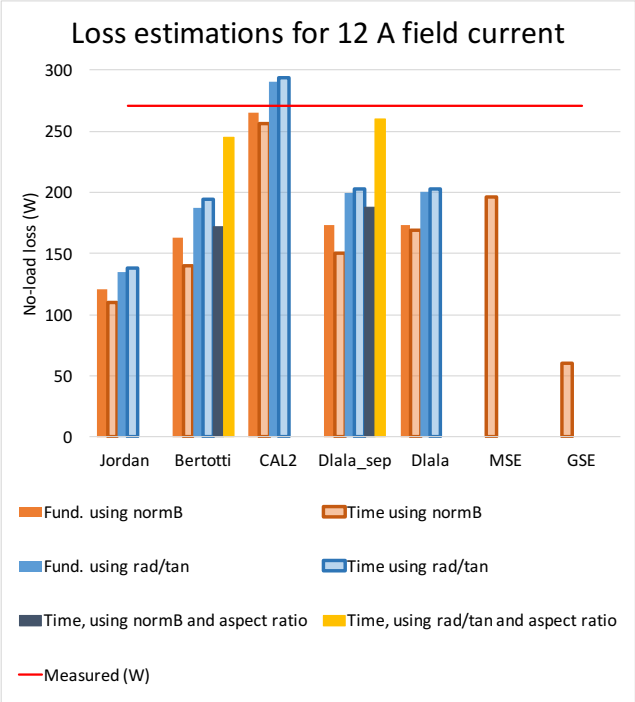

Fig. 39. Comparison of methods for 12 A field current

It is seen in figure 39 that all variations of the CAL2-method are close to the measured value. However, based on the tendency seen in figure 32 it is known that the CAL2 overestimates for higher flux densities (comparable to higher field current). Moreover it is seen that the Dlala

and the Dlala_sep methods are extremely similar in their predictions for all variations except the time domain version based on normB. This supports the previous indications that there is little change in accuracy when decomposing to three components instead of two. Comparing the Bertotti-method and the Dlala_sep method to the others, the large drop in estimated loss from fundamental to time domain when normB is used, seems to be characteristic for the three term methods. However, when replacing the normB by radial and tangential components, this trait seems to vanish completely, leaving all methods with a slightly higher estimation for time domain calculation compared to fundamental frequency calculation.

The percent-wise separation of loss components at 12 A field current is presented in figure 40. All numbers are calculated using radial and tangential components. It can be seen that the sum of classical eddy current components and anomalous losses for the three term methods do not at all correlate to the "dynamic losses" in the two term methods. Conversely, it seems that the anomalous loss components "draw " from both the dynamic and the hysteresis losses. This is not surprising as the models are just fitted by the least sum of error, and it is natural to pose the question of how much the separation of components can be related to their physical origin, as was acknowledged by Ionel [44] .

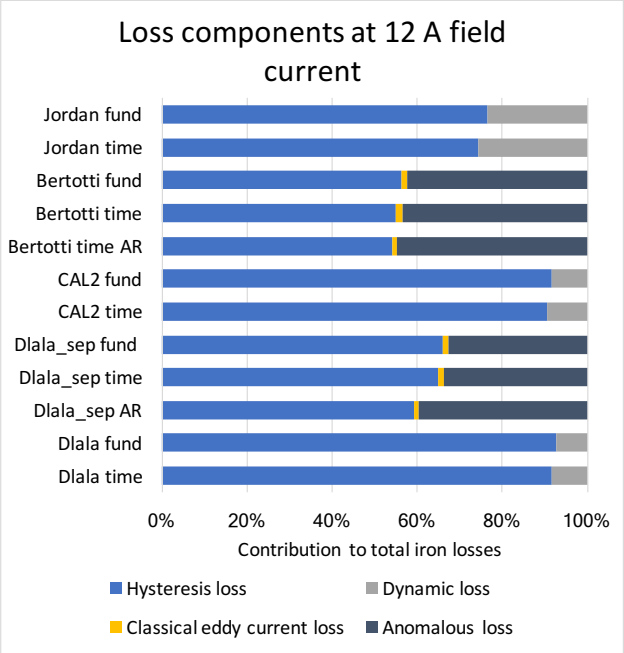

Fig. 40. Percentage contribution from the loss components for the methods evaluated at 12 A field winding current when radial and tangential compoenets are used

F. Loss density distribution

The loss density distribution for rotational and alternating losses are presented in figures 41 and 42 calculated by the Dlala_sep method including radial and tangential components and the aspect ratio. The rotational losses are highest behind the teeth, as expected from the distribution of the aspect ratio (figure 29). The alternating losses (figure 42) are highest in the teeth, and quite evenly distributed in the yoke. The zoomed picture of the teeth in the upper left corner of figure 42 shows the edges and corners of the teeth have highest alternating loss density, due to high flux density in these corners.

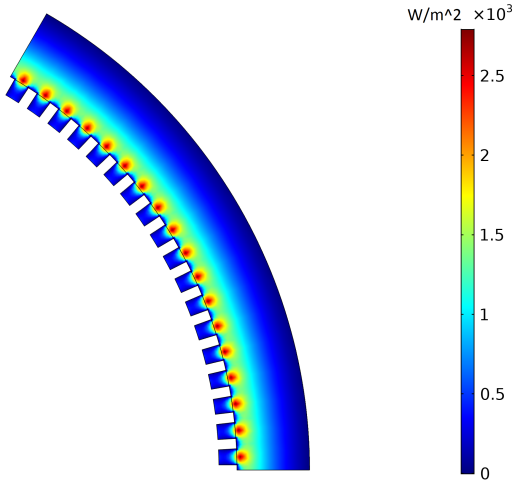

Fig. 41. Rotational losses for Dlala_sep with aspect ratio and radial/tangential components at 12 A field current, given in $\frac{W}{m^2}$

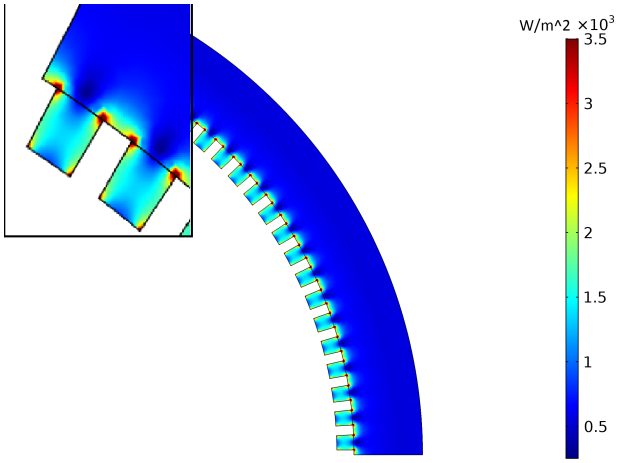

Fig. 42. Alternating losses for Dlala_sep with aspect ratio and radial/tangential components at 12 A field current, given in $\frac{W}{m^2}$

Figure 43 show the loss density distribution for radial and tangential components calculated by the Bertotti method. The radial losses are highest in the teeth, as expected, whereas the tangential losses are highest in the yoke. A high concentration of radial losses are seen in the tooth corners and high concentration of tangential losses is seen just behind the teeth. This correspons to the high degree of alternating losses in these areas seen in figure 42 However, compared to the rotational losses is figure 41, the "belt" of high loss density in the inner yoke is not observed in the tangential loss density, where the yoke losses are quite evenly distributed.

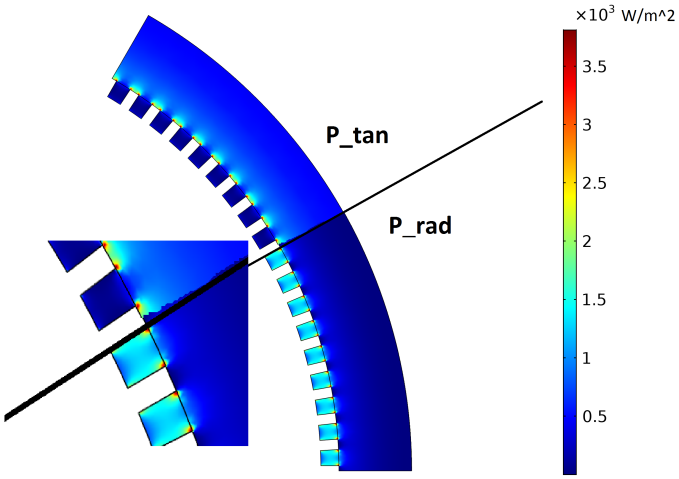

Fig. 43. Radial and tangential components of losses calculated by the Bertotti method in the time domain, given in $\frac{W}{m^2}$. A zoomed picture is given in the lower left corner, where higher loss densities are seen in the tooth back corners and behind the slots

G. Impact of mesh refinement

The effect of using a finer mesh and smaller time steps was investigated. A mesh of size *extremely fine* was selected for stator iron, and the number of time steps was increased to 1300 (10 times the original). Thus, the losses were recalculated for the 12 A field current case. The result was an average reduction of the loss prediction with 0.24 %, where no method showed a larger deviation than 0.37%. The coarse meshing is thereby concluded to have little impact on the accuracy of the calculation.

VIII. Implementation of methods for a high-speed compact PM motor

A COMSOL model for a high speed PM motor was developed for the project preceding this thesis [19]. The loss evaluation methods were also implemented for this model to evaluate behaviour for a different machine. This is to evaluate the general applicability of the models.

A. Machine data

The machine is a high speed permanent magnet synchronous machine with internal rotor analysed in [43]. It has a rated speed of 18 000 rpm and 4 poles. The input parameters used to create the model are given in table VII.

TABLE VII
Input parameters as given in article by Zhang et al. [43]

Item	Parameter	Item	Parameter
Rated power	1 MW	Rated speed	18 000 rpm
Current amplitude	355 A	Rated frequency	600 Hz
Stator outer diameter	550 mm	Stator core diameter	190 mm
Rotor outer diameter	184 mm	Air gap length	3 mm
Iron core length	400 mm	Slot number	27
Pole number	4	PM material	NdFeB
PM thickness	17 mm	PM conductivity	625000 S/m
Winding layers	2	Conductors per slot	6

The material used is named B20AT1500, for which material data was not publicly available. A corresponding material was therefore used for the analysis, named SURA Hi-Lite NO20. The material data can be found in appendix A11.

The stator iron losses predicted in [43] were 6116.8 W during full load at nominal speed. 91.8% of the losses were found to be caused by the fundamental frequency component, and 20 % of the losses from rotational loss. No specific iron loss measurements were performed, but the predicted values were verified through temperature measurements.

B. Model properties

1) Building the model: The model was made in 2D with rotating magnetic machinery physics. The geometry and the winding layout is presented in figure 44. The BH curve for the stator and rotor iron in the model was replaced by the data provided in the data sheet for Hi-Lite NO20 (appendix A11) at 400 Hz, which was the available data closest to nominal frequency. The model is excited with purely sinusoidal current. More in-depth information about the definitions in the COMSOL model can be found in the project report [19].

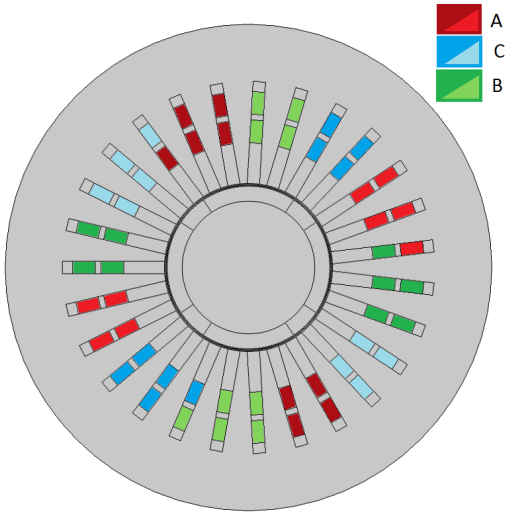

Fig. 44. Geometry and winding implementation for high speed machine. The darker colours indicate negative current direction

2) Model characteristics: The flux density for the machine at full load is seen in figure 45. Areas close to saturation are observed in the inner parts of the teeth.

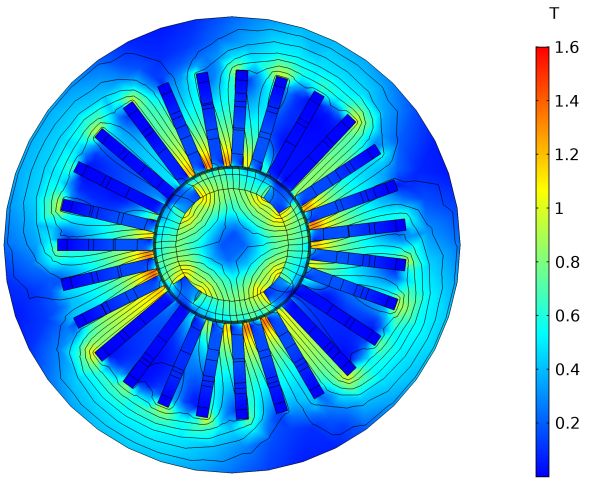

Fig. 45. Flux density distribution in the high speed machine

Cut points were set in the geometry to investigate some general properties. Figure 46 shows the selected cut points, where one is set in the center of a stator tooth, and one is set in the yoke.

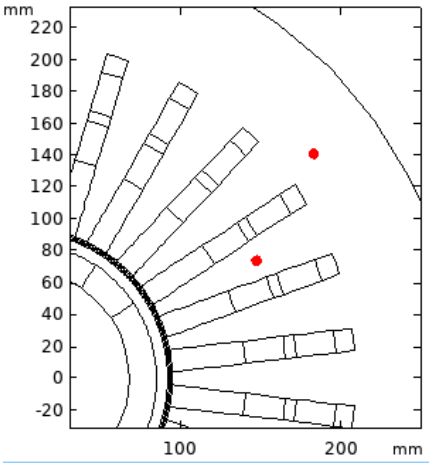

Fig. 46. Cut points in the geometry

Evaluating the radial and tangential flux density components in the cut points and using the built-in frequency spectrum transformation, figure 47 shows the degree of harmonics in the points. The fundamental component at 600 Hz is clearly dominant, however, contributions are seen for the third harmonic (1800 Hz), 5th harmonic (3000 Hz) and 7th harmonic (4200 Hz).

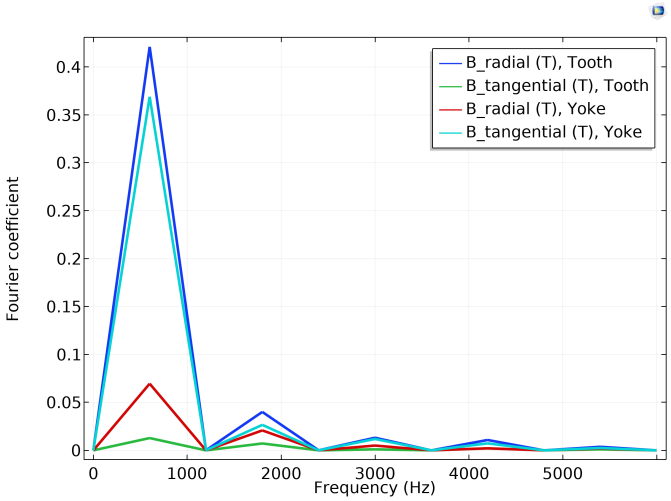

Fig. 47. Fourier transform of radial and tangential flux density components in the cut points

The aspect ratio was plotted to evaluate the degree of rotation in the machine, as seen in figure 48. It is seen that the highest degree of rotation is found above the stator teeth, as expected. However, no points in the machine seem to have any higher degree of circularity than 50%.

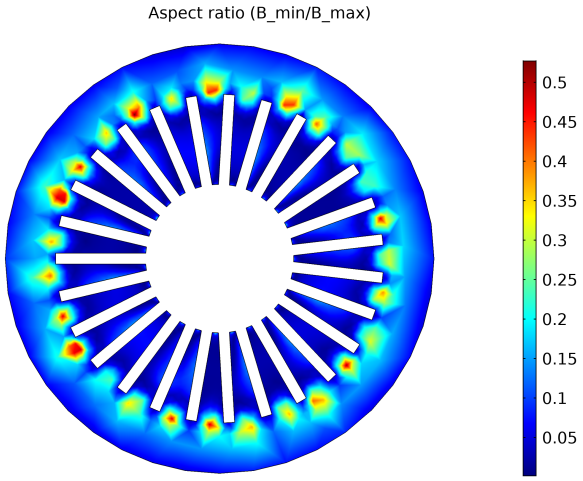

Fig. 48. Aspect ratio plotted over the surface of the high speed machine

C. Implementation of methods

Methods were implemented as described in section VI. As the closest available frequency in the data sheet is 400 Hz, this was used for the constant coefficient-fittings. For the Dlala coefficients, data for 50 Hz, 400 Hz and 2500 Hz was used. For this material, these are the lowest available frequencies. For the Dlala_sep method, only data for 50 Hz and 400 Hz was used, as the inclusion of the 2500 Hz data resulted in unrealistic numbers. Using only two frequency levels might be a source of inaccuracy.

The linear fitting for the Dlala-model is presented in figure 49. Surprisingly, the linear fit seems more accurate for this material than for the Cogent M530-50A used in the hydro

generator, even though data is drawn from a wide frequency range.

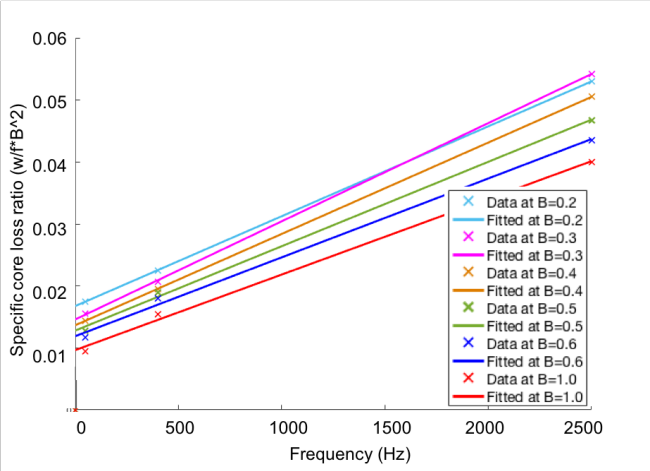

Fig. 49. Linear fit of loss density ratio for the Dlala-method

The resulting coefficients are presented in table VIII and figures 50, 51. For the hysteresis coefficients (figure 50), the constant Bertotti-coefficient is close to an averaged value of the variable coefficients. However, comparing the constant eddy current and anomalous loss coefficients in table VIII to the variable coefficients in figure 51, the constant coefficients are significantly lower for almost the entire range of flux densities. This is different than the results obtained for the hydro generator, where figure 26 showed the variable anomalous loss coefficient exceeded the constant one at approximately 0.5 T.

TABLE VIII
COEFFICIENTS FOR THE HIGH SPEED MACHINE

Method	Coefficient	Value
Bertotti	K_h	0.02497
Bertotti	K_e	1.6540e-05
Bertotti	K_a	2.831e-05
Steinmetz	C_{se}	0.3697
Steinmetz	α	0.6003
Steinmetz	β	1.781

The CAL2 and the Jordan model was not investigated due to difficulty finding appropriate coefficients based on the limited data.

The same R-curves used for the hydro generators are implemented in this model. This might be questionable due to the high operating frequency (600 Hz), as they are only valid when skin effect can be neglected. However, negligible skin effect is an assumption for loss separation overall.

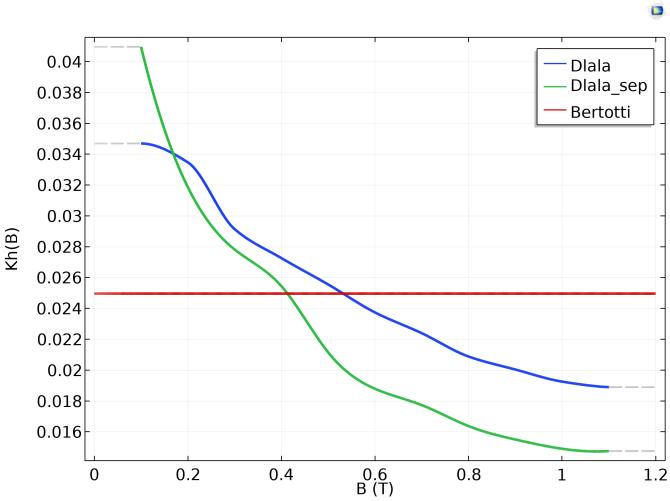

Fig. 50. Comparison of hysteresis coefficients fitted for the different methods

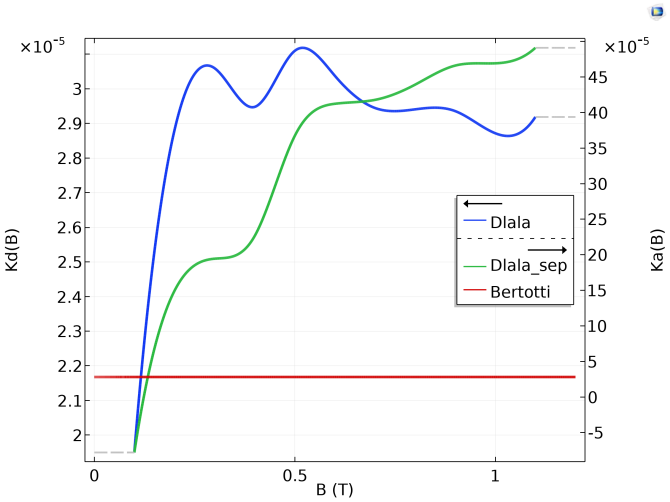

Fig. 51. Comparison of dynamic and anomalous coefficient fitted for the Dlala, the Dlala_sep and the Bertotti method

D. Results

The resulting loss evaluations for the high speed machine are presented in figure 52. A larger difference between the Bertotti and the Dlala results is seen for this machine compared to the hydro generator results. For this machine, the GSE is more accurate than the MSE, however both are far from the measured value. The Steinmetz-methods thereby seem to be very unpredictable in accuracy.

By dividing the losses found by the fundamental frequency by the respective time domain extension (for the evaluations including radial and tangential component), it was found that the share of losses generated by the fundamental component was 98%, 97% and 96 % respectively for the Bertotti, the Dlala_sep and the Dlala-methods. This is higher than what was found in the reference article (91.8%). The share of rotational losses was was 19% for both the Bertotti model and the Dlala_sep method (using for rad/tan components

combined with aspect ratio), corresponding well to the 20% found in [43].

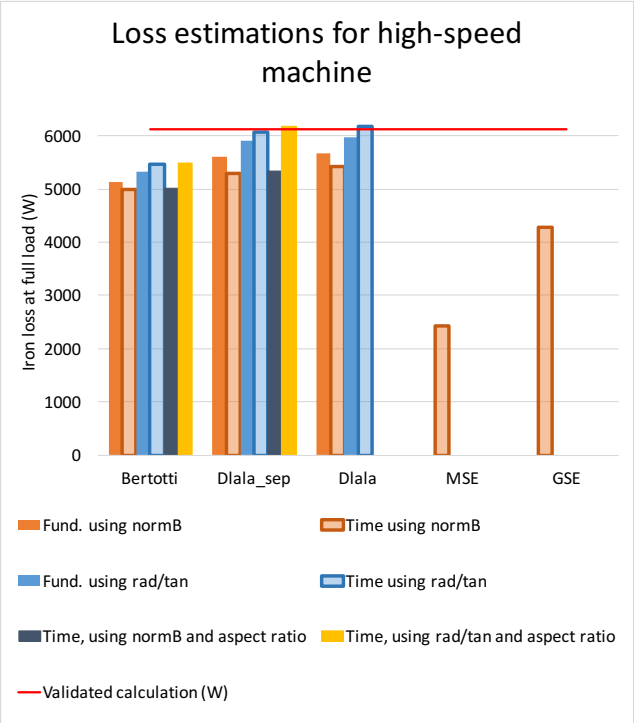

Fig. 52. Results of implemented methods for the high speed machine at full load and nominal speed

Table IX shows the increase by introducing radial and tangential components for the calcualtions in the high speed machine. It is seen that all methods have increased losses when radial and tangential components are used (relative to using normB), and the increase is two to three times as high for the time domain models compared to their corresponding fundamental implementation. However, the increase is lower than for the hydro generator (figure 33), where the increase for the time domain models was between 15%-50 %.

TABLE IX
INCREASE BY INTRODUCING RADIAL AND TANGENTIAL COMPONENTS RELATIVE TO NORMB

Method	Fund	Time
Bertotti	4 %	9 %
Dlala_sep	5 %	15 %
Dlala	5 %	14 %

Table X shows the relative error for the calculations using radial and tangential components. The Dlala_sep method has the lowest relative error for the time domain evaluations. A 1% overestimation is seen when including aspect ratio. The Bertotti method including aspect ratio resulted in 10 % underestimation.

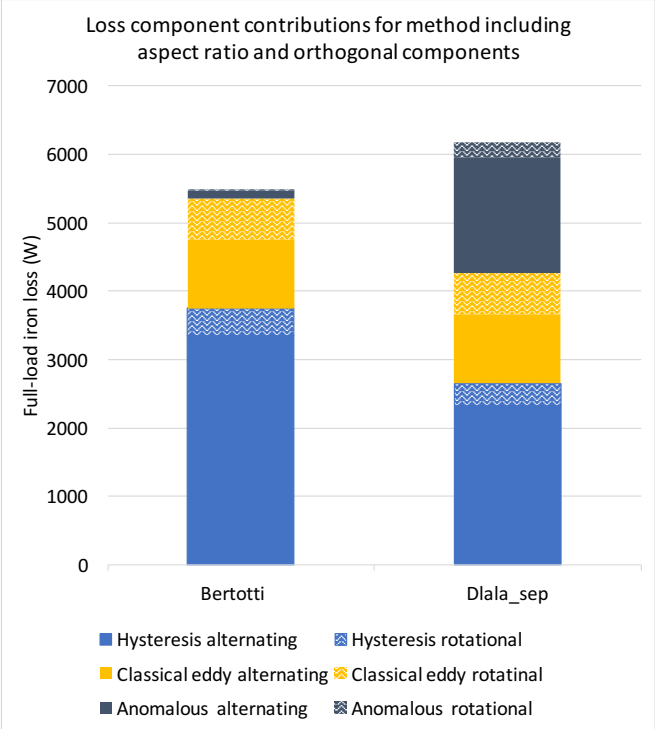

Fig. 53. Contribution from loss components for the methods using aspect ratio in combinations with radial and tangential compoenents

TABLE X
RELATIVE ERROR FOR METHODS USING RADIAL AND TANGENTIAL COMPONENTS

Method	Fund.	Time	Aspect ratio
Bertotti	-12.85 %	-10.73 %	-10.27 %
Dlala	-2.40 %	1.16%	
Dlala_sep	-3.50 %	-0.71 %	1.03 %
MSE		-60.34 %	
GSE		-29.90 %	

Figure 53 presents the contributions from the different loss components for the Bertotti and the Dlala_sep methods using radial and tangential components and aspect ratio. It is seen that the main difference between the two methods is the contribution from the anomalous loss component. Moreover, the hysteresis component is larger for Bertotti than for Dlala_sep.

IX. EVALUATION OF MODELLING RESULTS

A. The use of norm B

Judging by the large improvement in accuracy when including radial and tangential components, it is concluded that using *normB* is not appropriate for machines with a high degree of rotational flux.

Figure 33 and table IX showed the increase when including radial and tangential components was largest for the time domain models. The reason for this might be observed in figures 54 and 55. Figure 54 shows a comparison of

normB and the absolute value of the radial and tangential components for two selected points in the hydro generator. The two points are located behind a tooth (point 4) and a bit further out in the yoke (point 5). It has already been shown that these are points where the flux has a high degree of rotation (see figures 19 and 28). Figure 54 shows that the norm B does not vary very much in magnitude when the radial and tangential components are large (circular flux). This is particularly apparent for point 4.

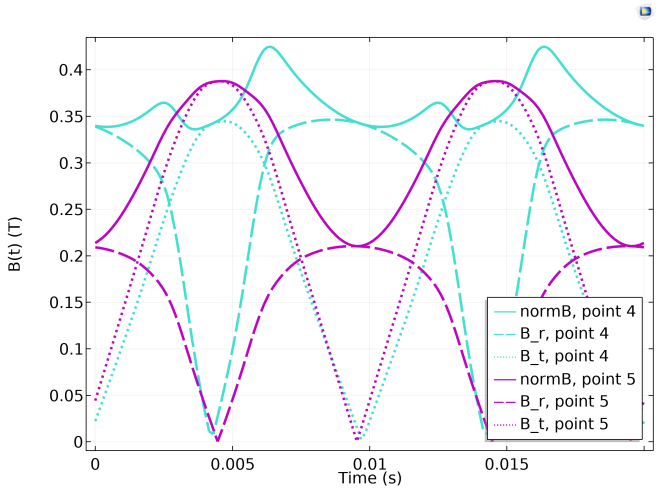

Fig. 54. Comparison of radial and tangential components and the normB for two points in the stator yoke

Further studying this aspect, figure 55 can be investigated. Figure 55 shows the squared time derivatives of the radial component, the tangential component and the normB. It is clear that the sum of the areas under the radial and tangential component curves is not equal to the area under the norm B curve. This indicates that

$$\int_0^T \left|\frac{dB_{norm}}{dt}\right|^2 \neq \int_0^T \left|\frac{dB_r}{dt}\right|^2 + \int_0^T \left|\frac{dB_t}{dt}\right|^2$$

for the points with a high degree of rotation. The same applies for the anomalous loss component, where the exponent 2 is replaced by 1.5. This might explain why the time domain solutions perform so poorly when normB is used.

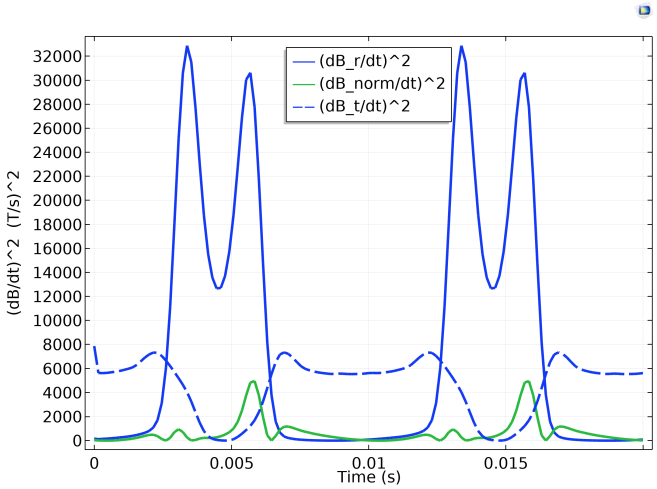

Fig. 55. Comparison of the square of the time derivative of flux vectors

B. Impact of flux loci circularity

The increase in loss prediction when introducing radial and tangential components for is much lower for the high speed machine (table IX) than for the hydro generator (figure 33). This might be related to the degree of flux loci circularity observed in the machine. Comparing the aspect ratio plots for the hydro generator (figure 29) and the high speed machine (figure 48), it seen that there is a much higher degree of rotation in the hydro generator. The high speed machine has spots just behind the teeth where the aspect ratio reaches 0.45-0.5 (45-50 % circular loci) in some of the spots. For the hydro generator, the spots behind every tooth reaches 0.7-0.8. Moreover, the hydro generator has a "belt" in the inner yoke, where the aspect ratio is around 0.5, whereas the high speed machine has aspect ratio about 0.25 around the concentrated points. This indicates that the hydro generator has a much larger percentage area of the machine where the rotational flux is highly significant, which might explain why the inclusion of radial and tangential components has more drastic results for the hydro generator.

C. Impact of flux density on rotational losses

The same tendency can be seen for the inclusion of aspect ratio and rotational loss density. Whereas the reduction in average relative error for the Dlala_sep method when including aspect ratio (both orthogonal components) is 21 %, the same difference in relative error is only 1.7% for the high speed machine. This is, as just described, related to the degree of circularity in the machine. However, it is also largely affected by the level of flux density in the machine. The R-curves in figure 6 show that the ratio of rotational loss versus alternating loss decrease for increasing flux densities. Studying the flux density plot for the hydro generator (figure 11) compared to the high speed machine (figure 45), it is seen that the flux density in the hydro generator yoke is overall much lower than in the high speed machine. The impact this has on rotational loss density can be seen by plotting the R-curves over the surface of the machines. Figure 56 shows the rotational hysteresis loss density for the hydro generator.

It is seen that the density is overall high, and at about 1.6 in "belt" where it is known the degree of rotation is about 50%. Comparing to figure 57 where the same R-curve is plotted over the surface of the high speed machine, it is seen that the spots with high degree of rotation coincide with spots of low rotational loss density due to higher induction levels. The same was found for the anomalous rotational loss density. This might explain why the increase in loss calculation is so much larger for the hydro generator than in the high speed machine when including aspect ratio. Moreover, it proves the R-curves as a flexible tool for loss calculation, adjusting to the conditions in the relevant machine.

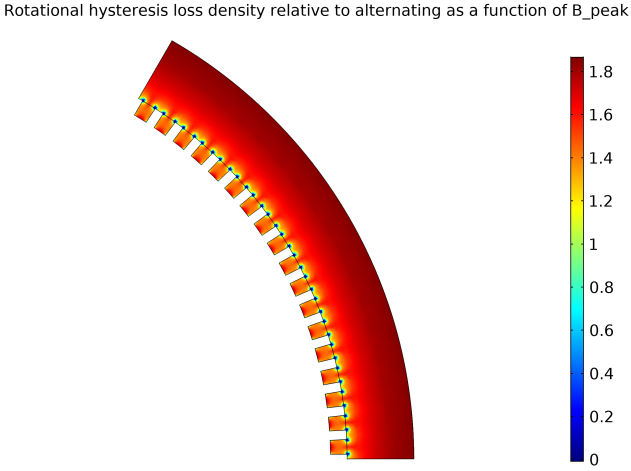

Fig. 56. Rotational hysteresis loss density for the hydro generator

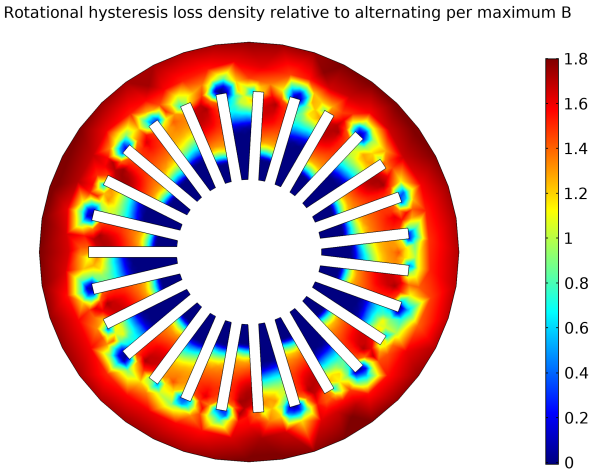

Fig. 57. Rotational hysteresis loss density for the high speed machine

D. Impact of component separation

Studying the contributions from the different loss components in the two machines, some tendencies can be seen. Figures 36 and 37 shows the contributions from the loss components for the Bertotti and the Dlala_sep methods respectively, for the hydro generator. A tendency was noted, where the contribution from the anomalous losses was much lower for Dlala_sep than for Bertotti at low field currents, but much higher for Dlala_sep than for Bertotti at higher field currents. This lead to overall similar total losses. However for the high speed machine, figure 53 shows the same tendency where Dlala_sep has larger anomalous loss component and lower hysteresis component than the Bertotti. However, the total sum is not equal in this case. This might be due to operation at higher frequency, where the contribution from the anomalous losses become far more significant. This might indicate that the separation of loss components has more impact for higher frequencies. However, it is difficult to evaluate too many tendencies for the high speed machine, as loss calculations have only been performed for one rotational speed. Moreover, the coefficients for the Dlala_sep method were fitted using only two frequency levels (50 and 400 Hz), which might be inaccurate. It should also be mentioned that the difference between the Dlala_sep anomalous coefficient and the Bertotti-coefficient is larger for the high speed machine than for the hydro generator (refer to figures 51 and 26), however it does not alone explain the difference.

The component separation is also seen to have impact on contribution from harmonics, as seen in figure 38 showing increased harmonic contribution for the variable coefficient methods when the field winding current increases. As a higher degree of dynamic components are seen for increasing field current (related to the increasing dynamic coefficients in figures 25 and 26), a higher degree of harmonics can exist. This also explains figure 33, where the increase by introducing radial and tangential components to the time domain models with variable coefficient was larger at higher field winding current. Thus, it is seen that the variable coefficients has impact on many aspects in the analysis.

E. Method for fitting of variable coefficients

Comparing the accuracy of the CAL2 method and the Dlala and Dlala_sep methods, it seems the point-wise method is more accurate over a wide range than the surface fit used in CAL2. Figure 32 shows that both Dlala methods follow the rate of increase for the measured losses, however with a steady underestimation, which is later corrected by the rotational loss density method (figure 35). The CAL2 has a much steeper rate of increase than the measured losses, indicating even larger over prediction for higher levels of induction than simulated in this work.

F. Data used for coefficient fitting

A source of inaccuracy for the high speed machine is that no data was available for the nominal frequency (600 Hz), leading to all coefficients being fitted to 400 Hz data. This seems to have little effect based on the accuracy of the calculations, but it is difficult to say how fitting to 600 Hz would have impacted coefficients. An observation is that the Dlala_sep method including rotational loss lead so a slight overestimation for the high speed machine, while an underestimation for the hydro generator. This might be due to the data used for coefficient fitting. It should also be investigated whether skin effect is negligible at this

level of frequency, which might have changed the separate contributions from the components.

However, another inaccuracy that is for all time domain models, is that the coefficient corresponding to fundamental frequency was used for all loss evaluations. This is an inaccuracy compared to using frequency domain models, as stated in section III-E.5. As harmonics seem to have small contributions in both analyses, this seems to not have affected the estimations greatly. However, this might have been interesting to compare, particularly in high speed machines where high fundamental frequency can generate high frequency harmonics.

Moreover, it is difficult to say how the accuracy for the implemented models had been affected if the fundamental was not so dominant, as all methods are largely fitted to data for the fundamental. As found in the literature review, using high frequencies in the coefficient fittings might dominate the solution [40]. This might be a reason for the large difference seen in Jordan and Bertotti models, and it is difficult to say whether the difference in accuracy is owning to the use of the anomalous loss term of the input data. However, use of the anomalous loss term allowed robust fit using only 50 Hz input, which was not possible for the two term expression (Jordan).

It should be discussed that the data used for coefficient fittings are not the actual material data for either of the analyses. Particularly for the hydro generator, where the material is unknown, the data sheet selected by Engevik [52] was selected based on similarity to measured specific losses. Thereby, the possible discrepancies caused by machining might be excluded from this analysis, as the input data might not accurately reflect the relation between supplier data and the assembled machine. However, it is difficult to say how using original data would affect the analysis. For the high speed machine, less insecurity is tied to this aspect, as the data was selected based on knowledge of the actual material used. It is uncertain how good the material data fits the actual machines, and whether errors induced by this could overshadow other tendencies in the results. However it is certain that the analysis largely relies on good material data for the iron, particularly the magnetisation curve and the specific losses.

G. The decreasing accuracy for low field current in the hydro generator

Figures 34 and 35 showed the accuracy of all models seemed to be significantly lower for low field winding current. This might be due to phenomena neglected in the analysis becoming more dominating when the stator iron losses are so low. Examples of this can be rotor losses and eddy currents due to leakage flux, as mention in section I. Engevik obtained similar discrepancy, and explained it by inaccuracies when separating very small iron losses from many times larger mechanical losses [52]. Another theory could be that the Dlala_sep-coefficients have a too steep increase for the increasing flux densities (thereby for increasing field winding current), so that if measurements were performed for higher flux densities in the machine, an overestimation would be seen. This is difficult to evaluate based on the presented results, but should be acknowledged.

H. The Steinmetz models

The Steinmetz implementations were seen to be unpredictable in accuracy. For the hydro generator, the MSE was the most accurate model when *normB* was used, with an average relative error of 38%, however increasing accuracy at nominal operation (figure 34). The GSE in the same machine was far less accurate, with an average error of 81%. The reason for this has not been clarified. The GSE is known to be less accurate when a third harmonic is significant [1], and third harmonics have been observed (figure 18). However, it is unclear in [1] what is meant by "significant", and whether the third harmonic observed in figure 18 can be considered a such, where the maximum magnitude of the third harmonic component is seen to be about 14% of the fundamental magnitude in the measuring points. The separate evaluation of equivalent frequency used in the MSE was found to be 221,31 Hz at 11 A field winding current and 224.83 Hz for 13 A current, which corresponds well to the findings in the Fourier transform (figure 18), and can be used as an indication of correct implementation. No such validation was performed for the GSE, and it cannot be ruled out that there is an error in the implementation. It might also be that the results had been better if coefficients were fitted to only 50 Hz data, but this cannot be concluded.

However for the high speed machine, the GSE was more accurate than the MSE, with respectively 29.90 % and 60.34% relative error. It should be mentioned this coefficient fitting was less accurate due to the limited amount of data, which might me a reason for the unexpected behaviour of the MSE. It is uncertain why the GSE performs so much better for this model.

I. Other sources of inaccuracy

The R-curve-extraction using MATLAB Grabit might be inaccurate. Ideally, these numbers should have been available in exact numbers. A last source of inaccuracy in the hydro generator model is that the air gap flux is found to be somewhat larger than the measured value (figures 14 and 15). This might have lead to higher loss predictions if flux densities are overall too high, and might therefore falsely make the methods seem overly accurate.

X. FURTHER WORK

For validation of the developed method using variable coefficients and rotational loss density (Dlala_sep), the method should be tested for more machines and variation of operating range. Further interesting work could be to extend the model for including minor loops.

XI. CONCLUSION

This thesis aimed to investigate iron loss calculation models for use in electrical machines, with focus on including low-frequency harmonics and rotational losses through

time-domain analysis. An extensive literature review has been conducted to obtain overview of existing methods, with focus on post-processing methods mainly within the concept of loss separation. A broad variation of practice has been discovered, where decisions regarding method are often based on application-specific requirements. This results in difficulty finding common ground for comparison of methods. Therefore, a benchmark FEM model was developed in COMSOL Multiphysics, where five variations of loss separation methods were implemented, focusing on method for coefficient determination and the use of the anomalous loss term.

The methods were further expanded to include rotational flux by calculation in radial and tangential direction, where a large improvement was seen. Moreover, by evaluating the degree of rotational flux per FEM element, the models using three loss terms were expanded to include rotational loss density by coupling generalized functions expressing the ratio of rotational loss relative to alternating loss per polarisation. This resulted in close agreement with measured losses, however slightly more accurate for the variable coefficient method. For comparison, three of the loss separation variations were implemented in a high speed permanent magnet machine model, where the variable coefficient method including anomalous component was superior. The Modified Steinmetz Equation (MSE) and the Generalized Steinmetz Equation (GSE) were also implemented in both cases, and showed fluctuating accuracy, overall lower than the previously described methods. These were not expanded to include rotation.

Main findings are listed below :

1) Variable coefficients seem to be more accurate than using constant coefficients, however might have more impact for machines operating at higher frequency, due to the separation of loss components having larger impact on the total sum of losses.
2) The point-wise methods for determining variable coefficients (Dlala, Dlala_sep) are more stable in accuracy than the direct surface fit (CAL2)
3) For machines with a high degree of rotational flux, the COMSOL built-in normB should not be used. This is particularly inaccurate in combination with time-domain analysis.
4) Including rotational losses through aspect ratio (degree of rotation) combined with rotational loss density curves seems to drastically increase accuracy, with 20-21% reduction in relative error for the hydro generator. Providing good overall accuracy for both hydro generator and high speed machine, this seems to be a flexible tool.

It should be remarked that the investigated methods are dependent on accurate material data, particularly the specific losses and the magnetization curve.

ACKNOWLEDGEMENTS

I would like to thank my supervisor Robert Nilsen for giving much inspiration and motivation for this work. Furthermore, I would also like to thank my co-supervisor Erlend Engevik in Rolls Royce for helping me both with the use of COMSOL, the progress of this thesis, and for always providing thorough answers to my questions. This thesis would never have been completed without your help. Moreover, I would like to thank Wei Wang for being very helpful to answer questions regarding implementation of methods in COMSOL. And lastly I would like to thank Jonas Nøland for the introduction to this topic and the use of COMSOL during the preparations in the previous semester.

REFERENCES

[1] A. Krings, "Iron losses in electrical machines — influence of material properties, manufacturing processes, and inverter operation," Doctoral thesis, Department of Electrical Energy Conversion, KTH School of Electrical Engineering, Stockholm, Sweden, April 2014.

[2] N. Boubaker, D. Matt, P. Enrici, F. Nierlich, and G. Durand, "Measurements of iron loss in pmsm stator cores based on cofe and sife lamination sheets and stemmed from different manufacturing processes," *IEEE Transactions on Magnetics*, vol. 55, no. 1, pp. 1–9, Jan 2019.

[3] J. Akiror, "Rotational core losses in hydro generators," Doctoral thesis, Department of Electrical and Computer Engineering, Concordia University, Montreal, Quebec, Canada, October 2016.

[4] Y. Guo, J. G. Zhu, J. Zhong, H. Lu, and J. X. Jin, "Measurement and modeling of rotational core losses of soft magnetic materials used in electrical machines: A review," *IEEE Transactions on Magnetics*, vol. 44, no. 2, pp. 279–291, 2008.

[5] Z. Zhu, S. Xue, W. Chu, J. Feng, S. Guo, Z. Chen, and J. Peng, "Evaluation of iron loss models in electrical machines," *IEEE Transactions on Industry Applications*, vol. 55, no. 2, pp. 1461–1472, 2019.

[6] S. Xue, Z. Q. Zhu, Y. Wang, J. Feng, S. Guo, Y. Li, Z. Chen, and J. Peng, "Thermal-loss coupling analysis of an electrical machine using the improved temperature-dependent iron loss model," *IEEE Transactions on Magnetics*, vol. 54, no. 11, pp. 1–5, 2018.

[7] D. Hanselman, *Brushless Permanent Magnet Motor Design*. Orono, ME, USA: The writers' collective, 2006.

[8] S. Xue, J. Feng, S. Guo, Z. Chen, J. Peng, W. Q. Chu, P. L. Xu, and Z. Q. Zhu, "Iron loss model for electrical machine fed by low switching frequency inverter," *IEEE Transactions on Magnetics*, vol. 53, no. 11, pp. 1–4, 2017.

[9] E. Barbisio, F. Fiorillo, and C. Ragusa, "Predicting loss in magnetic steels under arbitrary induction waveform and with minor hysteresis loops," *IEEE Transactions on Magnetics*, vol. 40, no. 4, pp. 1810–1819, July 2004.

[10] S. Hussain, M. H. Mohammadi, K. S. Sidhu, and D. A. Lowther, "Effects of pwm excitations on iron loss in electrical steels and machines," in *2017 IEEE Industry Applications Society Annual Meeting*, Oct 2017, pp. 1–8.

[11] J. Rens, S. Jacobs, and E. Attrazic, "Improved loss modelling of electrical traction motors by including magnetic skin effect," in *2018 IEEE International Conference on Electrical Systems for Aircraft, Railway, Ship Propulsion and Road Vehicles International Transportation Electrification Conference (ESARS-ITEC)*, 2018, pp. 1–6.

[12] M. Hofmann, H. Naumoski, U. Herr, and H. Herzog, "Magnetic properties of electrical steel sheets in respect of cutting: Micromagnetic analysis and macromagnetic modeling," *IEEE Transactions on Magnetics*, vol. 52, no. 2, pp. 1–14, Feb 2016.

[13] L. Vandenbossche, S. Jacobs, F. Henrotte, and K. Hameyer, "Impact of cut edges on magnetization curves and iron losses in e-machines for automotive traction," *World Electric Vehicle Journal*, vol. 4, pp. 587–596, 01 2011.

[14] A. Moses, N. Derebasi, G. Loisos, and A. Schoppa, "Aspects of the cut-edge effect stress on the power loss and flux density distribution in electrical steel sheets," *Journal of Magnetism and Magnetic Materials*, vol. 215-216, pp. 690 – 692, 2000. [Online]. Available: http://www.sciencedirect.com/science/article/pii/S0304885300002602

[15] A. Saleem, N. Alatawneh, R. R. Chromik, and D. A. Lowther, "Effect of shear cutting on microstructure and magnetic properties of non-oriented electrical steel," *IEEE Transactions on Magnetics*, vol. 52, no. 5, pp. 1–4, May 2016.

[16] A. Al-Timimy, G. Vakil, M. Degano, P. Giangrande, C. Gerada, and M. Galea, "Considerations on the effects that core material machining has on an electrical machine's performance," *IEEE Transactions on Energy Conversion*, vol. 33, no. 3, pp. 1154–1163, Sep. 2018.

[17] L. Vandenbossche, S. Jacobs, T. Lugand, and A. Schwery, "Improved calculation of iron losses in large salient-pole synchronous hydro-generators," in *2016 6th International Electric Drives Production Conference (EDPC)*, Nov 2016, pp. 253–260.

[18] IEC, "Iec 60404-2. magnetic materials – part 2: Methods of measurement of the magnetic properties of electrical steel strip and sheet by means of an epstein frame," 2008. [Online]. Available: https://bit.ly/2M8BOdM

[19] S. F. Haukvik, "Loss reduction in high-speed compact pm motors for more electric aircraft," Department of Electric Power Engineering, NTNU – Norwegian University of Science and Technology, Project report in TET4520, Dec. 2019.

[20] S. J. Chapman, *Electric machinery fundamentals*, 3rd ed. McGraw-Hill Boston, 1999. [Online]. Available: http://www.loc.gov/catdir/toc/mh022/98006407.html

[21] G. Bertotti, *Hysteresis in Magnetism: For physicists, materials scientists, and engineers*. Academic press, 1998.

[22] M. Albach, T. Durbaum, and A. Brockmeyer, "Calculating core losses in transformers for arbitrary magnetizing currents a comparison of different approaches," in *PESC Record. 27th Annual IEEE Power Electronics Specialists Conference*, vol. 2, 1996, pp. 1463–1468 vol.2.

[23] J. Reinert, A. Brockmeyer, and R. W. A. A. De Doncker, "Calculation of losses in ferro- and ferrimagnetic materials based on the modified steinmetz equation," *IEEE Transactions on Industry Applications*, vol. 37, no. 4, pp. 1055–1061, 2001.

[24] K. Venkatachalam, C. R. Sullivan, T. Abdallah, and H. Tacca, "Accurate prediction of ferrite core loss with nonsinusoidal waveforms using only steinmetz parameters," in *2002 IEEE Workshop on Computers in Power Electronics, 2002. Proceedings.*, 2002, pp. 36–41.

[25] G. Bertotti, "General properties of power losses in soft ferromagnetic materials," *IEEE Transactions on Magnetics*, vol. 24, no. 1, pp. 621–630, Jan 1988.

[26] G. Bertotti, A. Boglietti, M. Chiampi, D. Chiarabaglio, F. Fiorillo, and M. Lazzari, "An improved estimation of iron losses in rotating electrical machines," *IEEE Transactions on Magnetics*, vol. 27, no. 6, pp. 5007–5009, Nov 1991.

[27] F. Fiorillo and A. Novikov, "An improved approach to power losses in magnetic laminations under nonsinusoidal induction waveform," *IEEE Transactions on Magnetics*, vol. 26, no. 5, pp. 2904–2910, Sep. 1990.

[28] P. A. Hargreaves, B. C. Mecrow, and R. Hall, "Calculation of iron loss in electrical generators using finite-element analysis," *IEEE Transactions on Industry Applications*, vol. 48, no. 5, pp. 1460–1466, Sep. 2012.

[29] E. Dlala, "Comparison of models for estimating magnetic core losses in electrical machines using the finite-element method," *IEEE Transactions on Magnetics*, vol. 45, no. 2, pp. 716–725, Feb 2009.

[30] D. Jiles and D. Atherton, "Theory of ferromagnetic hysteresis," *Journal of Magnetism and Magnetic Materials*, vol. 62, no. 1-2, pp. 48–60, September 1986.

[31] I. Mayergoyz, *Mathematical models of hysteresis and their applications*. New York, NY, USA: Elsevier Science, 2003.

[32] A. Ramesh, D. C. Jiles, and J. M. Roderick, "A model of anisotropic anhysteretic magnetization," *IEEE Transactions on Magnetics*, vol. 32, no. 5, pp. 4234–4236, Sep. 1996.

[33] A. J. Bergqvist, "A simple vector generalization of the jiles-atherton model of hysteresis," *IEEE Transactions on Magnetics*, vol. 32, no. 5, pp. 4213–4215, Sep. 1996.

[34] G. Bramerdorfer and D. Andessner, "Accurate and easy-to-obtain iron loss model for electric machine design," *IEEE Transactions on Industrial Electronics*, vol. 64, no. 3, pp. 2530–2537, March 2017.

[35] L. Chang, T. M. Jahns, and R. Blissenbach, "Generalized dynamic hysteresis model for improved iron loss estimation of complex flux waveforms," *IEEE Transactions on Magnetics*, vol. 55, no. 7, pp. 1–13, July 2019.

[36] M. Fratila, A. Benabou, A. Tounzi, and M. Dessoude, "Iron loss calculation in a synchronous generator using finite element analysis," *IEEE Transactions on Energy Conversion*, vol. 32, no. 2, pp. 640–648, June 2017.

[37] J. Ziske and R. Disselnkötter, "Modeling of anisotropic laminated magnetic cores using homogenization approaches," *Excerpt from the Proceedings of the 2014 COMSOL Conference in Cambridge*. [Online]. Available: https://bit.ly/39QyOwp

[38] J. Gyselinck and P. Dular, "A time-domain homogenization technique for laminated iron cores in 3-d finite-element models," *IEEE Transactions on Magnetics*, vol. 40, no. 2, pp. 856–859, March 2004.

[39] E. Dlala, A. Belahcen, and A. Arkkio, "On the importance of incorporating iron losses in the magnetic field solution of electrical machines," *IEEE Transactions on Magnetics*, vol. 46, no. 8, pp. 3101–3104, Aug 2010.

[40] J. Juergens, B. Ponick, O. Winter, and A. Fricassè, "Influences of iron loss coefficients estimation on the prediction of iron losses for variable speed motors," in *2015 IEEE International Electric Machines Drives Conference (IEMDC)*, May 2015, pp. 1254–1259.

[41] D. Kowal, P. Sergeant, L. Dupré, and L. Vandenbossche, "Comparison of iron loss models for electrical machines with different frequency domain and time domain methods for excess loss prediction," *IEEE Transactions on Magnetics*, vol. 51, no. 1, pp. 1–10, Jan 2015.

[42] Y. Huang, J. Dong, J. Zhu, and Y. Guo, "Core loss modeling for permanent-magnet motor based on flux variation locus and finite-element method," *IEEE Transactions on Magnetics*, vol. 48, no. 2, pp. 1023–1026, 2012.

[43] Y. Zhang, S. McLoone, W. Cao, F. Qiu, and C. Gerada, "Power loss and thermal analysis of a mw high-speed permanent magnet synchronous machine," *IEEE Transactions on Energy Conversion*, vol. 32, no. 4, pp. 1468–1478, Dec 2017.

[44] D. M. Ionel, M. Popescu, M. I. McGilp, T. J. E. Miller, S. J. Dellinger, and R. J. Heideman, "Computation of core losses in electrical machines using improved models for laminated steel," *IEEE Transactions on Industry Applications*, vol. 43, no. 6, pp. 1554–1564, Nov 2007.

[45] E. Dlala, M. Solveson, S. Stanton, and A. Arkkio, "Improved model for the prediction of core loss in finite element analysis of electric machines," in *2015 IEEE International Electric Machines Drives Conference (IEMDC)*, 2015, pp. 340–344.

[46] D. Kowal, P. Sergeant, L. Dupré, and H. Karmaker, "Comparison of frequency and time-domain iron and magnet loss modeling including pwm harmonics in a pmsg for a wind energy application," *IEEE Transactions on Energy Conversion*, vol. 30, no. 2, pp. 476–486, June 2015.

[47] T. H. Akinaga, T. Staudt, W. Hoffmann, C. E. Soares, A. A. de Espíndola, and J. P. A. Bastos, "A comparative investigation of iron loss models for electrical machine design using fea and experimental validation," in *2018 XIII International Conference on Electrical Machines (ICEM)*, Sep. 2018, pp. 461–466.

[48] C. Appino, M. Khan, O. de la Barrière, C. Ragusa, and F. Fiorillo, "Alternating and rotational losses up to magnetic saturation in non-oriented steel sheets," *IEEE Transactions on Magnetics*, vol. 52, no. 5, pp. 1–4, 2016.

[49] S. Yue, Y. Li, Q. Yang, K. Zhang, and C. Zhang, "Comprehensive investigation of magnetic properties for fe–si steel under alternating and rotational magnetizations up to kilohertz range," *IEEE Transactions on Magnetics*, vol. 55, no. 7, pp. 1–5, 2019.

[50] M. Ranlof, A. Wolfbrandt, J. Lidenholm, and U. Lundin, "Core loss prediction in large hydropower generators: Influence of rotational fields," *IEEE Transactions on Magnetics*, vol. 45, no. 8, pp. 3200–3206, 2009.

[51] Lei Ma, M. Sanada, S. Morimoto, and Y. Takeda, "Prediction of iron loss in rotating machines with rotational loss included," *IEEE Transactions on Magnetics*, vol. 39, no. 4, pp. 2036–2041, 2003.

[52] E. Engevik, "Design and operation investigations for large converter-fed synchronous machines in hydropower applications," Thesis for the Degree of Philosophiae Doctor, Department of Electric Power Engineering, NTNU – Norwegian University of Science and Technology, June 2019. [Online]. Available: https://ntnuopen.ntnu.no/ntnu-xmlui/handle/11250/2604881

[53] EMETOR, "Electric motor winding calculator." [Online]. Available: https://www.emetor.com/windings/

[54] COMSOL, *COMSOL Multiphysics User's Guide*, 2012.

[55] ——, *COMSOL Multiphysics Reference Manual*, 2019.

[56] jiro, "Grabit, matlab central file exchange." 2016. [Online]. Available: https://se.mathworks.com/matlabcentral/fileexchange/7173-grabit

APPENDIX

A. Input data for hydro generator simulations

TABLE A1

BH CURVE FOR STATOR IRON IN HYDRO GENERATOR MEASURED AT UPPSALA UNIVERISTY

"H (A_per_meter)"	"B (tesla)"
0	0
73	0.80000000000000004
80	0.84999999999999998
89	0.90000000000000002
100	0.94999999999999996
113	1
130	1.05
149	1.1000000000000001
173	1.1499999999999999
205	1.2
257	1.25
336	1.3
410	1.3500000000000001
536	1.3999999999999999
752	1.45
1368	1.5
2234	1.55
3363	1.6000000000000001
4332	1.6499999999999999
6042	1.7
8892	1.75
13338	1.8
18354	1.8500000000000001
24054	1.8999999999999999
34181	1.95
50739	2

TABLE A2

BH CURVE FOR ROTOR IRON IN HYDRO GENERATOR MEASURED AT UPPSALA UNIVERISTY

"H (A_per_meter)"	"B (tesla)"
0	0
144.321	0.83999999999999997
159.40700000000001	0.89249999999999996
178.41300000000001	0.94499999999999995
202.55699999999999	0.99750000000000005
235.46100000000001	1.05
286.91800000000001	1.1025
346.77300000000002	1.155
442.95499999999998	1.2075
604.87900000000002	1.26
892.43600000000004	1.3125
1492.97	1.365
2416.96	1.4175
3596.0599999999999	1.47
5278.9499999999998	1.5225
7480.7299999999996	1.575
10259.799999999999	1.6274999999999999
14032.6	1.6799999999999999
19565.599999999999	1.7324999999999999
31427.700000000001	1.7849999999999999
58221.400000000001	1.8374999999999999
92283.899900000004	1.8899999999999999
125601	1.9424999999999999

Typical data for SURA® M530-50A

T	W/kg at 50 Hz	VA/kg at 50 Hz	A/m at 50 Hz	W/kg at 100 Hz	W/kg at 200 Hz	W/kg at 400 Hz
0,1	0,04	0,11	56,1	0,14	0,23	0,56
0,2	0,14	0,31	74,1	0,42	0,82	2,07
0,3	0,30	0,54	85,8	0,81	1,70	4,29
0,4	0,48	0,81	95,6	1,24	2,80	7,09
0,5	0,69	1,10	105	1,58	4,09	10,5
0,6	0,92	1,43	114	2,14	5,56	14,6
0,7	1,17	1,80	123	2,83	7,20	19,5
0,8	1,44	2,20	133	3,49	9,09	25,5
0,9	1,74	2,65	145	4,28	11,3	32,6
1,0	2,07	3,15	158	5,52	13,8	40,8
1,1	2,43	3,75	174	6,46	16,7	50,4
1,2	2,84	4,48	200	7,38	20,0	61,5
1,3	3,30	5,48	243	8,73	23,8	74,1
1,4	3,84	7,06	333	10,2	28,2	89,1
1,5	4,46	10,8	573	12,0	32,8	105
1,6	5,16	23,6	1345			
1,7	5,81	62,3	3367			
1,8	6,30	144	6964			

Loss at 1.5 T , 50 Hz, W/kg	4,46
Loss at 1.0 T , 50 Hz, W/kg	2,07
Anisotropy of loss, %	6
Magnetic polarization at 50 Hz	
H = 2500 A/m, T	1,63
H = 5000 A/m, T	1,71
H = 10000 A/m, T	1,83
Coercivity (DC), A/m	85
Relative permeability at 1.5 T	1600
Resistivity, μΩcm	31
Yield strength, N/mm²	245
Tensile strength, N/mm²	385
Young's modulus, RD, N/mm²	210000
Young's modulus, TD, N/mm²	220000
Hardness HV5 (VPN)	120

RD represents the rolling direction
TD represents the transverse direction
Values for yield strength (0.2 % proof strength)
and tensile strength are given for the rolling direction
Values for the transverse direction are approximately 5% higher

cogent
Surahammars Bruks AB

June 2008

Fig. A4. Material data used for loss evaluations in hydro generator

B. Implementation in COMSOL

TABLE B3

GLOBAL PARAMETERS DEFINED IN COMSOL

Do	"876 [mm]"	"Stator outer diameter"
Di	725[mm]	"Stator inner diameter"
delta0	"8.4 [mm]"	"Airgap width"
lm	"303 [mm]"	"Machine length"
hpb	"134 [mm]"	"Pole body height"
wpb	"74 [mm]"	"Pole body width"
hps	"20 [mm]"	"Pole shoe height"
ht	"15 [mm]"	"Tooth height"
Dri	"231.8 [mm]"	"Rotor inner diameter"
Dpi	"391 [mm]"	"Pole inner diameter"
wps	"131.36 [mm]"	"Pole shoe width"
fwh	"122 [mm]"	"Field winding coil height"
fww	"2.8 [mm]"	"Field winding coil width"
ws	8.5[mm]	"Slot width"
cw	"6.5 [mm]"	"Coil width"
w	"50*pi/3 [rad/s]"	"Angular velocity"
ia	"0 [A]"	"Phase A current"
ib	"0 [A]"	"Phase B current"
ic	"0 [A]"	"Phase C current"
fw	16[A]	"Field winding current"
nt	162	"Number of turns"
f	"50 [Hz]"	"Rated frequency"
kh_CAL2_0	0.11	"polynomial coefficient for CAL2 function"
kh_CAL2_1	-0.1747	""
kh_CAL2_2	0.1322	""
kh_CAL2_3	-0.03402	""
kc_CAL2_0	0.0001218	"polynomial coefficient for CAL2 function"
kc_CAL2_1	6.541e-06	""
kc_CAL2_2	5.849e-05	""
kc_CAL2_3	-1.47e-05	""
rho	"7650 [kg/m^3]"	"Material density "
KhJ	0.03197	"Kh Jordan (50-400 Hz as input)"
KcJ	0.0001964	"Kc Jordan (50-400 Hz as input)"
Ke_an	1.6128e-5	"Ke analytical"
T	1/f	"Electrical period"
Kh_B	0.03278	"Kh Bertotti"
Ka_B	0.002046	"Ka Bertotti"
C_se	0.003022	"Steinmetz coefficient C"
a_se	1.592	"Steinmetz coefficient alpha"
b_se	2.213	"Steinmetz coefficient beta"

TABLE B4

LOCAL VARIABLES DEFINED IN COMSOL UNDER COMPONENT->DEFINITIONS->VARIABLES

phi2	attimemax(0, T, rmm.normB, atan(rmm.By/rmm.Bx))	"angle for major axis relative to x axis"
B_min	rmm.Bx*cos(phi2)+rmm.By*sin(phi2)	B_minor
B_maj	rmm.Bx*sin(phi2)-rmm.By*cos(phi2)	B_major
B_r_p	timemax(0, T, B_r , 'nointerp')	"B_radial peak value"
B_t_p	timemax(0, T , B_t, 'nointerp')	"B_tangential peak value"
B_n_p	timemax(0, T , rmm.normB, 'nointerp')	"B_norm peak"
rot_ratio	timemin(0,T, rmm.normB, 'nointerp')/timemax(0, T , rmm.normB , 'nointerp')	"Degree of rotation (Bmin/Bmax)"
eddyInt_n	timeint(0, T , abs(d(rmm.normB , TIME))	
textasciicircum2)	"Integral in eddy current loss evaluation using normB"	
deltaB	timemax(0, T , rmm.normB, 'nointerp')-timemin(0 ,T , rmm.normB , 'nointerp')	"peak-peak value of normB"
dB_n	d(rmm.normB, TIME)	"Time derivative of normB"
B_r	(rmm.Bx*X+rmm.By*Y)/sqrt(X^2+Y^2)	B_radial
B_t	(rmm.Bx*Y-rmm.By*X)/sqrt(X^2+Y^2)	B_tangential

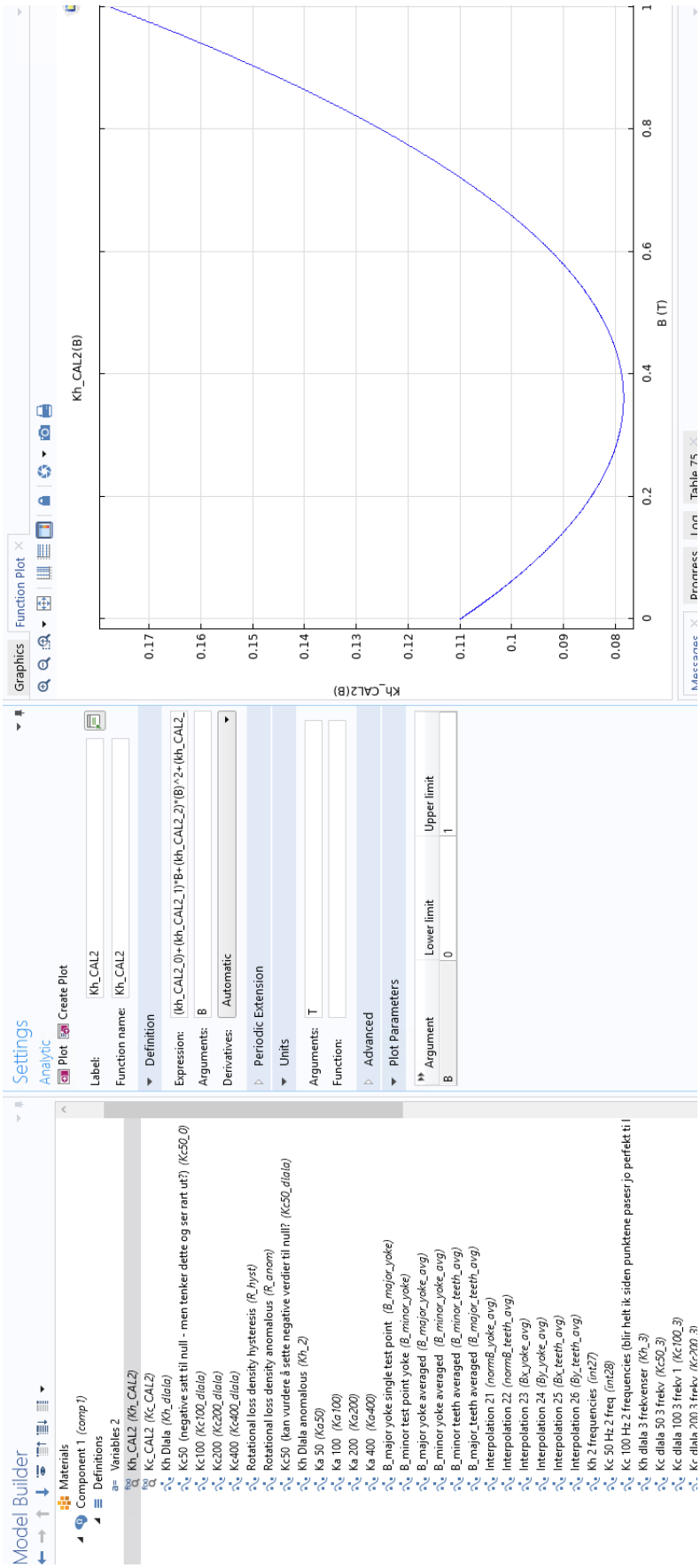

Fig. B5. CAL2 hysteresis coefficients implementation for hydro generator

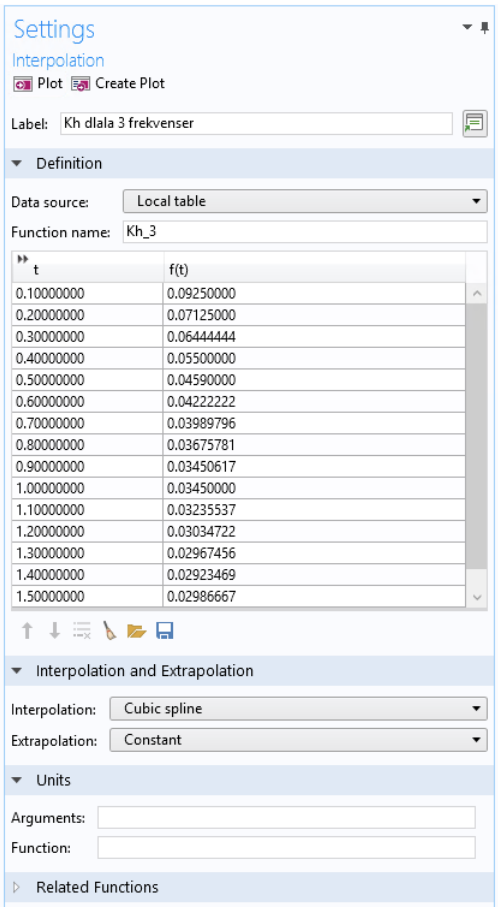

Fig. B6. Dlala hysteresis coefficients implementation for hydro generator

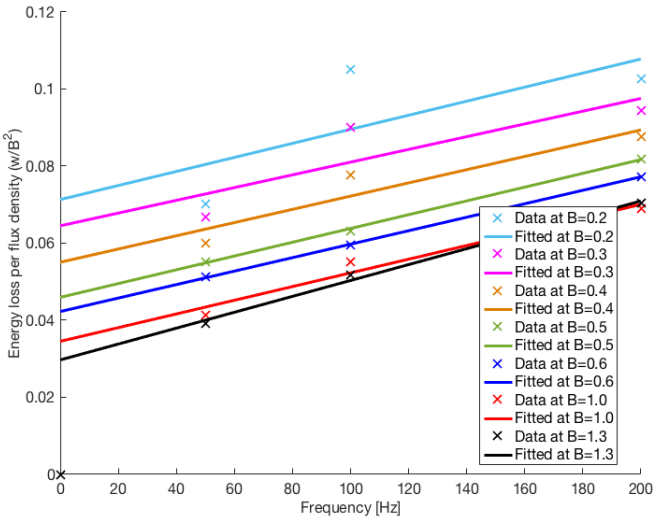

Fig. B7. Linear fit of loss density ratio when frequency range 50 Hz-200 Hz is used

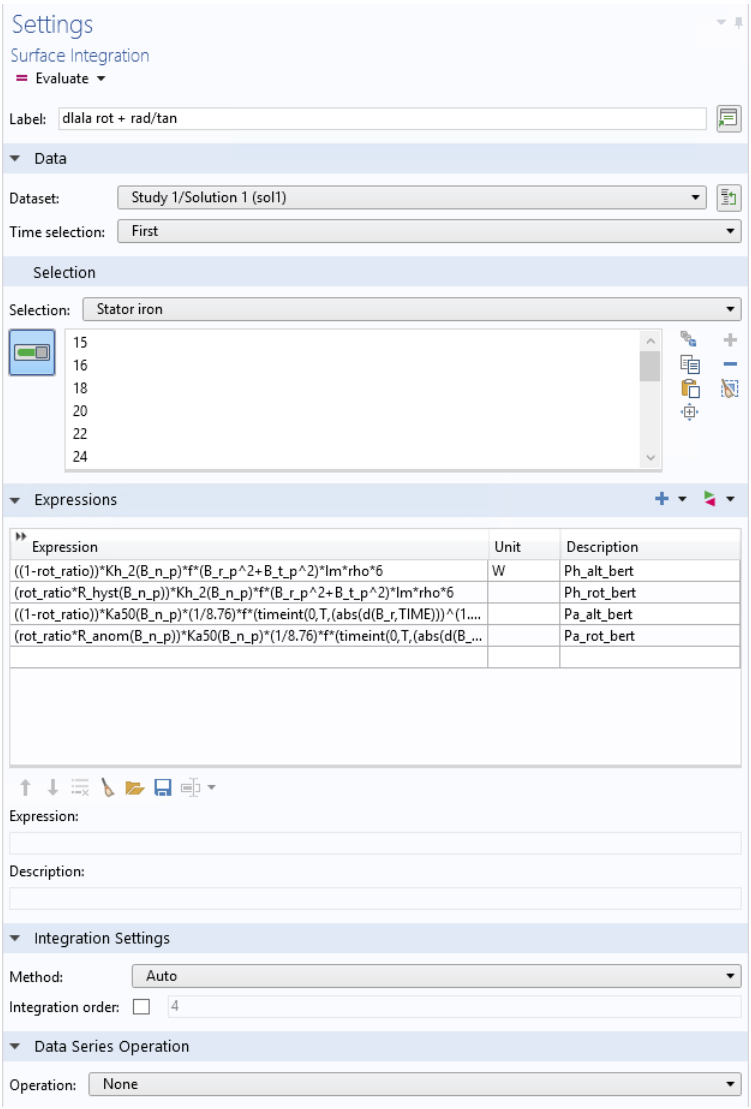

Fig. B8. Example of evaluation implemented in the surface integration. Here for the Dlala_sep method including rad/tan comopenents and aspect ratio

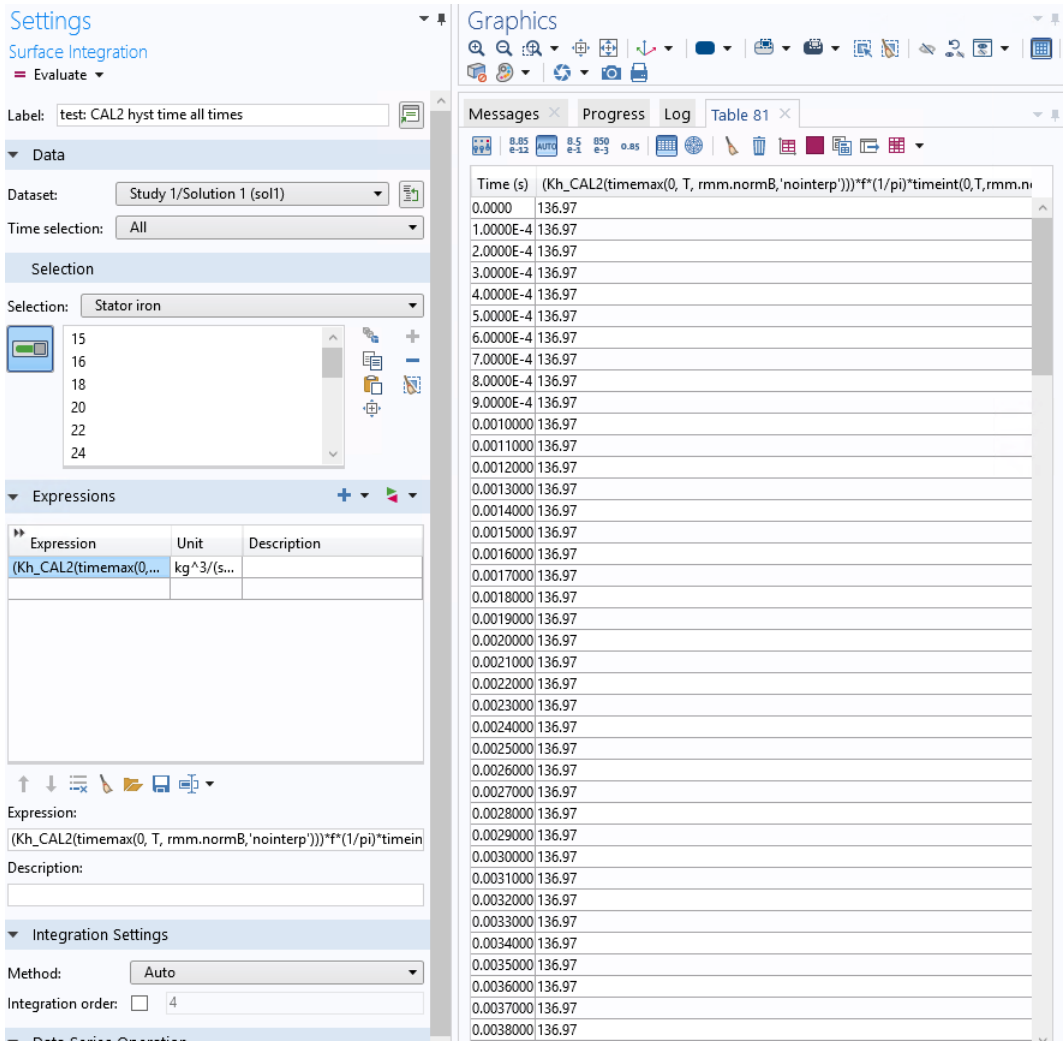

Fig. B9. Example of COMSOL outputting the same result for all time steps inducing extremely high computational time

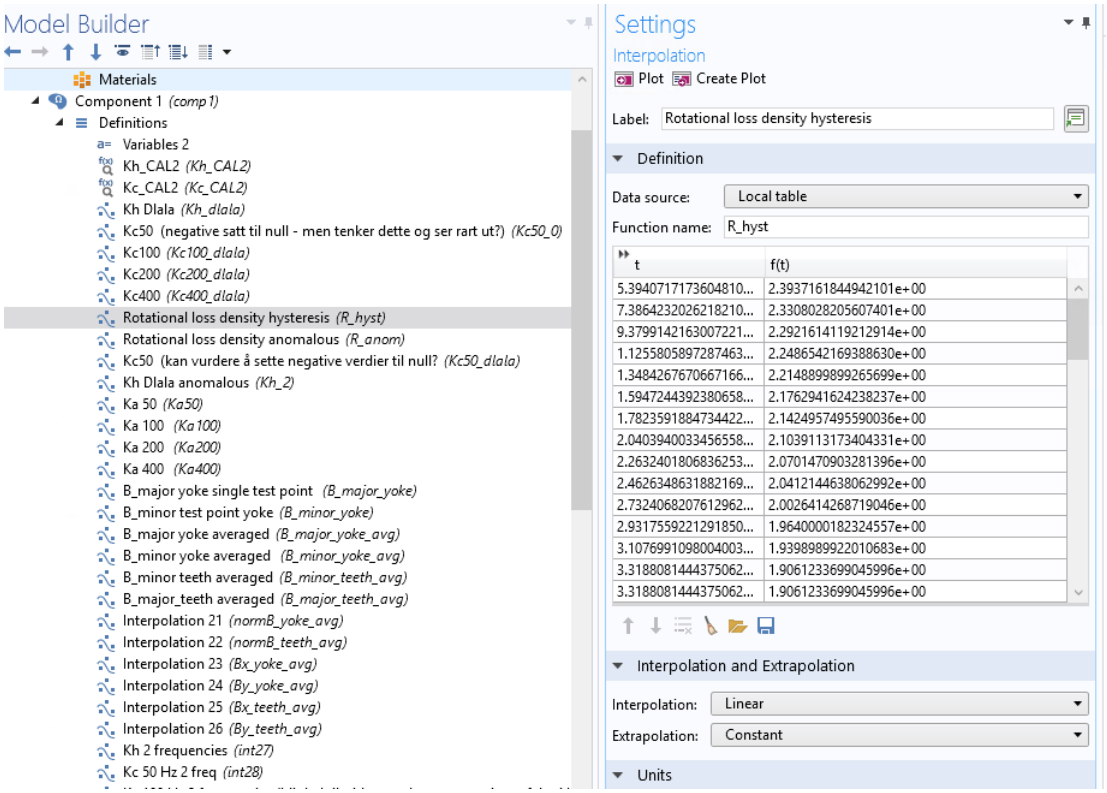

Fig. B10. R-curve for rotational hysteresis loss density implementation

C. Input data for high speed machine simulations

HI-LITE™
HIGH PERFORMANCE - ULTRA LIGHT

Apr 2015

NO20

TYPICAL VALUES

POLARISATION	SPECIFIC TOTAL LOSS				
J_{peak} T	at 50 Hz W/kg	at 400 Hz W/kg	at 2500 Hz W/kg	at 5000 Hz W/kg	at 10000 Hz W/kg
0.1	0.02	0.17	2.79	9.01	27.0
0.2	0.07	0.72	10.6	31.8	95.6
0.3	0.14	1.49	24.4	65.6	191
0.4	0.23	2.50	40.4	108	315
0.5	0.32	3.80	58.4	159	
0.6	0.42	5.17	78.4	219	
0.7	0.54	6.70	103	290	
0.8	0.66	8.36	133	375	
0.9	0.80	10.3	166	477	
1.0	0.95	12.3	200		
1.1	1.14	14.8	248		
1.2	1.36	17.9			
1.3	1.65	21.4			
1.4	2.00	25.3			
1.5	2.40	29.7			
1.6	2.75				
1.7	3.06				
1.8	3.32				

	GUARANTEED VALUES	TYPICAL VALUES
Loss at 1.0 T and 50 Hz, W/kg	-	0.95
Loss at 1.0 T and 400 Hz, W/kg	15.0	12.3
Loss at 1.0 T and 2500 Hz, W/kg	215	200
Nominal thickness, mm		0.20
Resistivity, μΩcm		52
Density, g/cm^3		7.65
Yield strength, N/mm^2		370
Tensile strength, N/mm^2		450
Young's modulus, RD, N/mm^2		185 000
Young's modulus, TD, N/mm^2		200 000
Hardness HV5		180

RD represents the rolling direction
TD represents the transverse direction
Values for yield strength (0.2 % proof strength)
and tensile strength are given for the rolling direction
Values for the transverse direction are approximately 5% higher

cogent
Surahammars Bruks AB

Fig. A11. Material data used for loss evaluations in high speed machine

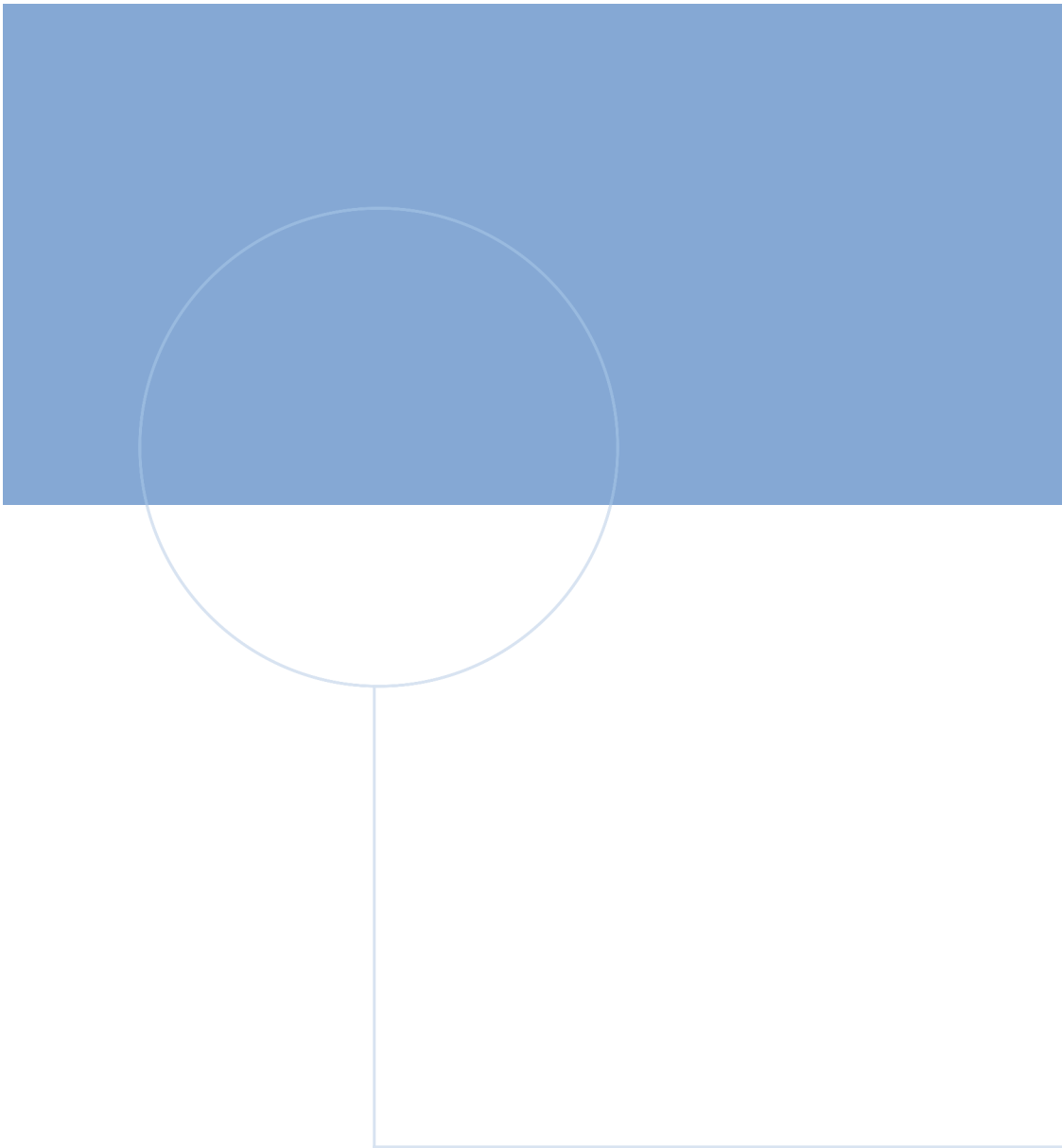

NTNU

Kunnskap for en bedre verden